TURBIDITY-BASED AERIAL PERSPECTIVE RENDERING FOR MIXED REALITY

大気混濁係数に基づいた複合現実感のための空気遠近法レンダリング

BY

CARLOS EMANUEL MORALES ESPINOZA

A MASTER DISSERTATION

SUBMITTED TO THE GRADUATE SCHOOL OF
THE UNIVERSITY OF TOKYO

IN PARTIAL FULFILLMENT OF THE REQUIREMENTS

FOR THE DEGREE OF

MASTER OF ELECTRICAL ENGINEERING AND INFORMATION SYSTEMS

FEBRUARY 2014

Thesis Supervisor: Takeshi OISHI　大石 岳史

ABSTRACT

Rendering realistic scenes is one of the most significant objectives in outdoor Mixed Reality (MR) applications that are created by merging virtual objects into real scenes. One type of these applications consists on rendering a virtual object in a position that is distant from the observer. The goal in such applications is to realistically model the natural atmospheric effect of the real scene over the virtual object's appearance. This natural phenomenon over distant objects in open air scenes is called aerial perspective and makes the object's color turn fainter and shift towards the environmental light color. Nevertheless, aerial perspective modeling is challenging because outdoor illumination is unpredictable and changes arbitrarily. In computer vision (CV) and computer graphics (CG), the light scattering phenomena that cause the aerial perspective effect are generally modeled by a combination of a directly transmitted light and an airlight. While Preetham *et al*. (1999) performed a study using such model and rendered a turbidity-based aerial perspective for complete-virtual applications, only Zhao (2012) has carried out a research applied to MR. Zhao used a simple adjustment of Preetham's aerial perspective model, however, only analyzed one atmospheric case and obtained a compute-intensive rendering. In this work, we propose an enhanced MR-directed scattering model using a full-spectrum turbidity-based approach and formulate an improved aerial perspective rendering model. For this purpose, we first estimate turbidity by matching the luminance distributions of a captured omnidirectional image and sky models. Then we employ the estimated turbidity to render a virtual object with aerial perspective effect.

Acknowledgements

First and foremost, I would like to acknowledge to my thesis supervisor, Prof. Takeshi Oishi, for his consideration and supervision. I am also grateful to Prof. Katsushi Ikeuchi for his help and advice during my research.

I offer deeply regards to all the members of the Computer Vision Laboratory and the Interaction Technology Laboratory of the University of Tokyo. Thank you for your support not only in academic matters but also in daily life.

Last but not least, I want to pay my highest tribute to my family. I dedicate this dissertation to all of you.

February 2014

Carlos Morales

Contents

List of Figures

List of Tables

Chapter 1

Introduction

1.1 Background

Mixed Reality (MR) finds several important applications in areas such as the academy, cultural heritage, entertainment, and so on. In outdoor MR that consists on integrating virtual objects into real scenes, one of the main goals is to create real-time applications where the appearance of the inserted virtual object corresponds to the real scene's look. In real open-air scenes, when a target object viewed by an observer is far, the perceived object's appearance changes losing contrast and blending with the environmental color. This natural effect is known as *aerial perspective* and is due to the light scattered by particles suspended in the atmosphere. Therefore, in outdoor MR applications where the target virtual object is distant from the observer, we need to render an artificial aerial perspective over the virtual object to emulate the natural atmospheric effect. Figure 1.1 illustrates a general MR scheme where an observer is watching a real scene of Tokyo city using a head mounted display (HMD). In the middle image of Figure 1.1, the MR application renders a virtual Mount Fuji behind the real mountains affected by the natural atmospheric effect. As it can be noticed in the bottom image of Figure 1.1, a synthesized aerial perspective effect has been rendered over the virtual Mount Fuji to generate a more realistic appearance. In practice, however, the aerial perspective rendering presents challenging issues due to the changing and unpredictable natural atmospheric phenomena such as the environmental illumination and weather conditions.

In order to provide a smooth understanding of the present thesis, in this section we explain background concepts on scattering in the atmosphere, atmospheric conditions via the parameter called *turbidity*, aerial perspective phenomena and its modeling, and the virtual object rendering model in MR.

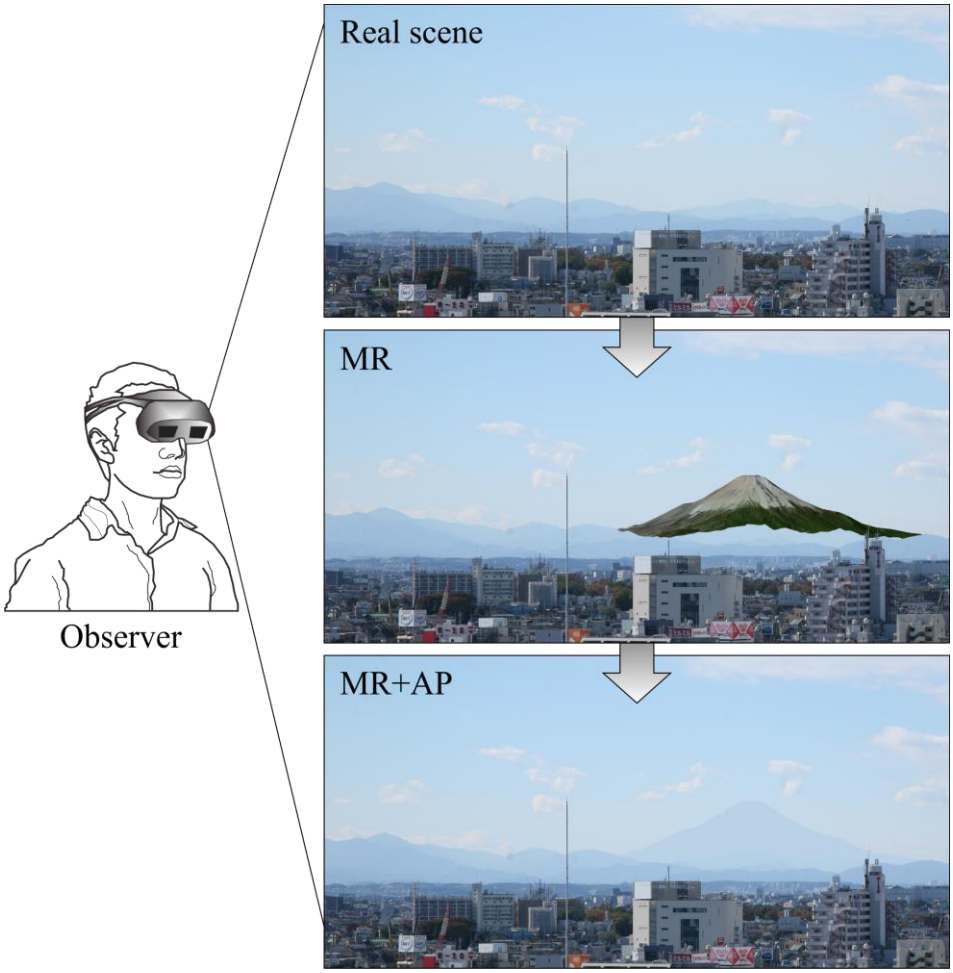

Figure 1.1. Mixed Reality (MR) scheme. Image in the top is real scene of Tokyo city. Image in the middle is MR with virtual Mount Fuji rendered. Image in the bottom is MR with aerial perspective (AP) effect rendered over the virtual Mount Fuji.

1.1.1. Scattering in the Atmosphere

Propagation of light through the atmosphere is governed by the scattering phenomena caused by the particles suspended in the atmosphere (Minnaert, 1954; McCartney, 1975; Lynch and Livingston, 1995). Figure 1.2 illustrates a collimated beam of light with radiance L ($W \cdot sr^{-1} \cdot m^{-3}$) traveling a distance s trough a scattering medium. This beam will lose part of itself due to the scattering out of the transmission path x. Then the remaining light of this beam is modeled by

$$L(s,\lambda) = L_0(\lambda) e^{-t_{sc}(s,\lambda)}, \tag{1.1}$$

where L_0 is the radiance at x=0 and t_{sc} is the optical thickness of the atmospheric path, and $e^{-t_{sc}(s,\lambda)}$ is called *attenuation factor*.

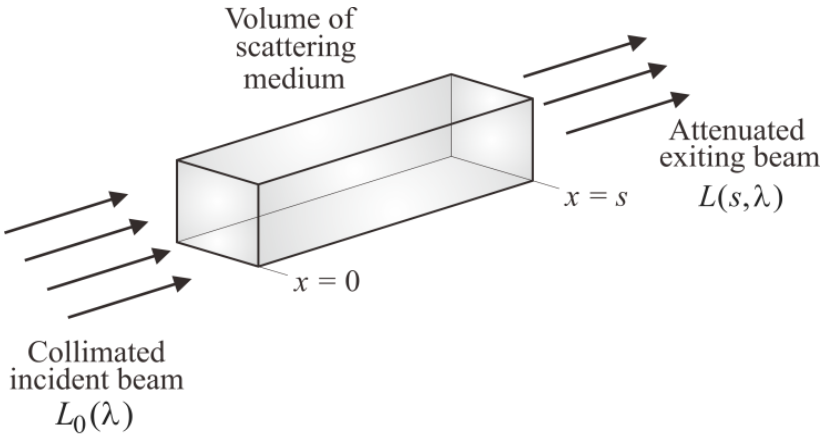

Figure 1.2. Scattering of a collimated beam of light through a volume of scattering medium.

In fact, the optical thickness conveys the total combined scattering effect of all the particles along the path *x*, and its value is expressed by

$$t_{sc}(s,\lambda) = \int_0^s \beta_{sc}(x,\lambda)dx\,, \tag{1.2}$$

where β_{sc} is called *scattering coefficient*.

The scattering coefficient is essensial in atmospheric scattering modeling since it contains information of the atmosphere such as the size and type of particles that are suspended in there and in which amount they scatter light. However, this coefficient depends not only on the atmospheric condition but also on the wavelengths of the incident light coming from the environment. In the past, Rayleigh (1871) and Mie (1908) studied the atmospheric scattering caused by small and larger particles respectively.

Rayleigh Scattering: Rayleigh (1871) studied the scattering of electromagnetic waves by particles much smaller than the electromagnetic wavelength "λ". Particles that fit into this category are, for instance, air molecules whose diameter is around 0.1 nm as shown in Table 1.1. At height *h* from sea level, the Rayleigh scattering coefficient is given by

$$\beta_R = \frac{8\pi^3(n^2-1)^2}{3N\lambda^4}\left(\frac{6+3p_n}{6-7p_n}\right)\times e^{\frac{-h}{H_0}}\,, \tag{1.3}$$

where n=1.0003 is the refractive index of air in the visible spectrum, p_n=0.035 is the depolarization factor for air, H_0=7994m is the scale height for small particles, and N=2.545×$10^{25}$$m^{-3}$ is the molecular number density of the standard atmosphere.

Using Equation (1.1), (1.2), and (1.3) we can deduce that short (blue) wavelengths will be more scattered than high (red) wavelengths in a pure air weather condition, thus explaining the reason why the sky is blue in such atmospheric conditions.

Table 1.1. Weather conditions and related particle types, sizes, and concentrations (Adapted from McCartney, 1975).

Condition	Particle type	Radius (μm)	Concentration (m^{-3})
Pure air	Molecule	10^{-4}	10^{25}
Haze	Aerosol	$10^{-2} - 1$	$10^{9} - 10^{7}$
Fog	Water droplet	$1 - 10$	$10^{8} - 10^{7}$

Mie Scattering: Mie (1908) studied the scattering by particles whose size is nearly equal to the wavelength of the electromagnetic wave. In atmospheric optics, we can use Mie scattering for particles such as aerosols and water drops. At height h from sea level, the Mie scattering coefficient is given by

$$\beta_M = 0.434c(T)\pi\left(\frac{2\pi}{\lambda}\right)^{v-2} K(\lambda)\times e^{\frac{-h}{H_0}}, \tag{1.4}$$

where c is the concentration factor that depends on the atmospheric turbidity, v=4 is the Junge's exponent, K is the wavelength-dependent Fudge factor, and H_0=1200m is the scale height for larger particles.

Using Equation (1.1), (1.2), and (1.4) we can deduce that short (blue) wavelengths and high (red) wavelengths scatter almost uniformily under hazy conditions, thus explaining the reason why aerosol particles creating haze make a whiteing of the normal blue sky color.

1.1.2. Atmospheric Condition via Turbidity

Turbidity: Turbidity (T) or atmospheric turbidity is defined as the ratio of the optical thickness of the atmosphere composed by molecules of air (t_R) plus larger particles (t_M) to the optical thickness of air molecules alone (McCartney, 1975):

$$T = \frac{t_R + t_M}{t_R}, \tag{1.5}$$

where t_R and t_M are calculated using Equations (1.2), (1.3) and (1.4) for the Rayleigh and Mie scattering coefficients respectively.

In practice, turbidity is used to express a quantitative and straightforward characterization of atmospheric conditions, as shown in Figure 1.3. For instance, using turbidity we can classify skies for atmospheric conditions in a very clear day (T=1.8), in a clear day (T=3), in a slightly hazy day (T=6), or even in cloudy days.

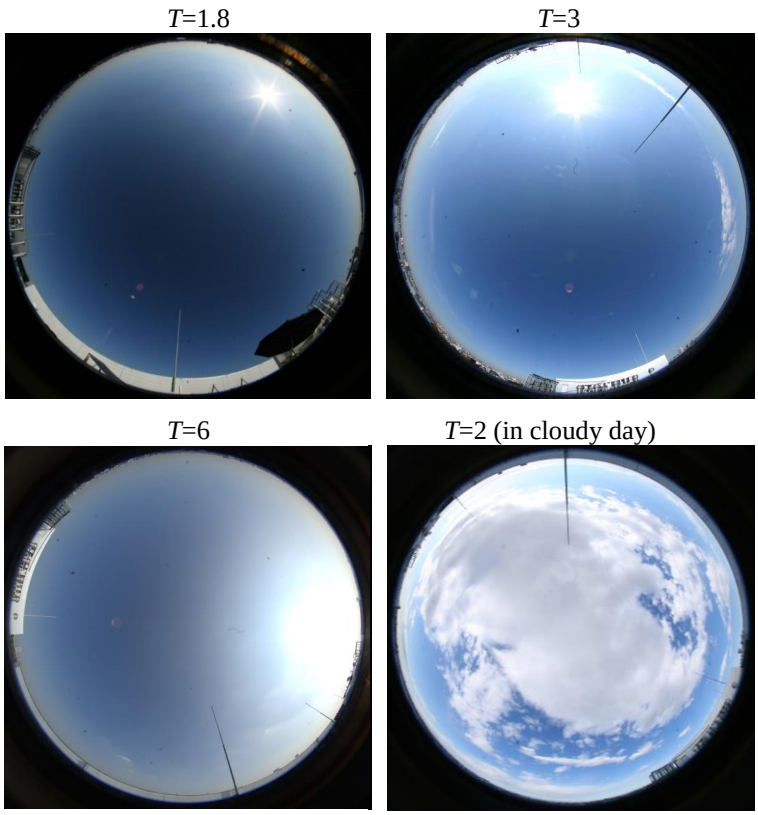

Figure 1.3. Panoramic sky-dome images captured by Canon EOS 5D with fish eye lens.

The Preetham Sky Model: Due to the importance of the relation *weather condition* versus *turbidity*, turbidity-based sky models have been widely used in CG. Preetham *et al*. (1999) presented an analytical sky model for various atmospheric conditions through turbidity. The sky can be represented through the coordinates of the upper sky hemisphere, as illustrated in Figure 1.4. In that sky coordinates the observer is located in the *xyz* origin, θ is the zenith angle of viewing direction V, θ_s is the zenith angle of the sun position, and γ is the angle of the sun direction with respect to the viewing direction. Based on this coordinates, the Preetham sky model relates the luminance Y_V (cd/m^2) of the sky in any

viewing direction with respect to the luminance at a reference point Y_z (in this case the zenith) by

$$\frac{Y_V}{Y_z} = \frac{F(\theta, \gamma, T)}{F(0, \theta_s, T)}, \tag{1.6}$$

where $F(\theta,\gamma)$ is the sky luminance distribution model of Perez *et al*. (1993) given by

$$F(\theta,\gamma) = \left(1 + Ae^{B/\cos\theta}\right)\left(1 + Ce^{D\gamma} + E\cos^2\gamma\right). \tag{1.7}$$

One of the most important contributions of the Preetham sky model is that he related the five distribution coefficients in Equation (1.7) and linearly modeld them via the turbidity parameter for the *Y* channel of the *xyY* color space as

$$\begin{bmatrix} A \\ B \\ C \\ D \\ E \end{bmatrix} = \begin{bmatrix} 0.1787 & -1.4630 \\ -0.3554 & 0.4275 \\ -0.0227 & 5.3251 \\ 0.1206 & -2.5771 \\ -0.0670 & 0.3703 \end{bmatrix} \begin{bmatrix} T \\ 1 \end{bmatrix}, \tag{1.8}$$

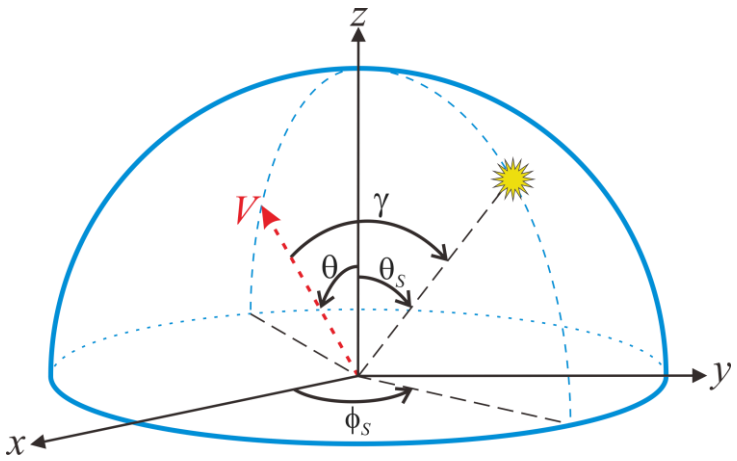

Figure 1.4. Coordinates in the sky hemisphere.

1.1.3. Aerial Perspective Modeling

Aerial perspective effect is caused due to the scattering of light by particles suspended in the atmosphere. In CV, the following scattering model is widely used in dealing with outdoor scenarios under various weather conditions (Narasimhan and Nayar, 2003; Fattal, 2008; Tan, 2008; Kratz and Nishino, 2009; He *et al*., 2009; Meng *et al*., 2013):

$$L(s,\lambda) = L(0,\lambda)e^{-\beta_{sc}(\lambda)s} + L(\infty,\lambda)(1 - e^{-\beta_{sc}(\lambda)s}). \tag{1.9}$$

In this equation, $L(s,\lambda)$ is the total light perceived by the observer. As we can notice, Equation (1.9) has mainly two components. These components are called *direct transmission* and *airlight*, and are illustrated in Figure 1.5. Regarding the first term, direct transmission refers to the light from the target, $L(0,\lambda)$, that is not scattered as it travels through the viewing path until reaching the observer. The second term is the airlight and stands for the environmental illumination, $L(\infty,\lambda)$, that is scattered into the direct transmission path and then is attenuated in the way to the observer. Finally, $\beta_{sc}=\beta_R+\beta_M$ is the total scattering coefficient, which is a summation of the Raileigh and Mie scattering coefficients, and s is the distance between the target and the observer.

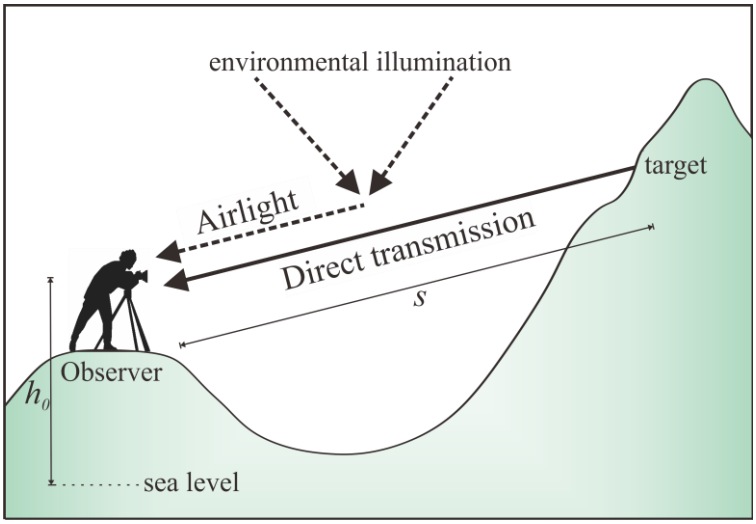

Figure 1.5. Aerial perspective described by direct transmission and airlight componets.

1.1.4. Virtual Object Rendering

For rendering a virtual object in MR applications, we need an equation to go from the radiometric formulas such as the spectral radiance to pixel color values such as RGB. In general, when an object is illuminated by a source of light, the reflected light goes through the camera lens used for capturing the scene and is recorded by its charged couple device (CCD). Then the recorded image intensity for the channel c∈{r,g,b} is obtained as

$$I_c = \int_{380\text{nm}}^{780\text{nm}} L(\lambda) q_c(\lambda) d\lambda \,, \tag{1.10}$$

where $L(\lambda)$ is the reflected spectral radiance at the object surface, 380 to 780nm stands for the visible spectrum of light, and $q_c(\lambda)$ is the spectral sensitivity of the camera.

Camera's spectral sensitivity: This parameter is important not only for going from radiance to RGB but also for color correction of the virtual object since it compensates the effects of the recording illumination. In this matter, Zhao (2012) used a turbidity-based method to calculate the spectral sensitivity of several cameras, so we will benefit from his data. Figures 1.6 illustrate spectral sensitivities for cameras Ladybug2 and Canon EOS 5D used in this thesis.

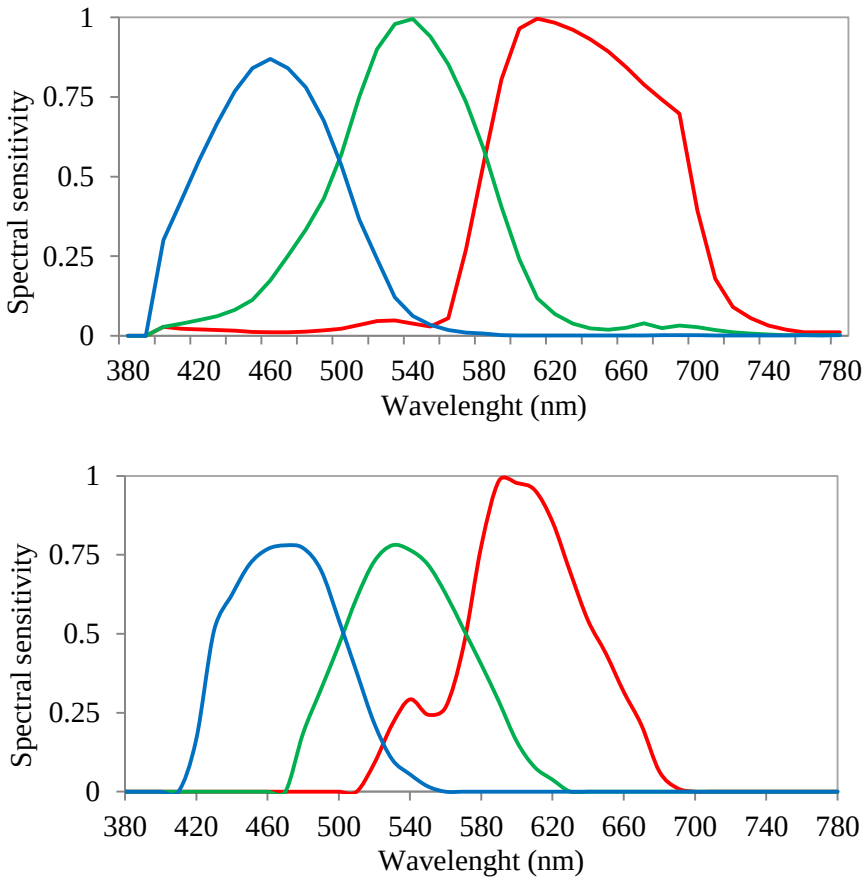

Figure 1.6. Spectral sensitivities from Zhao (2012) for cameras Ladybug2 (top) and Canon EOS 5D (bottom). Colors red, blue, and green stand for R, G, and B channels respectively.

1.2 Related Works

In this section we show some works related to modeling atmospheric optics. These works include reviews on scattering modeling, aerial perspective rendering for complete-virtual environments, aerial perspective rendering over virtual objects for MR applications, and fog modeling.

Common methods for aerial perspective modeling rely on understanding the scattering phenomena in the atmosphere. Such models vary depending on whether the aim is oriented to computer vision (CV) or computer graphics (CG). Here we summarize the most representative works in outdoor scattering modeling and aerial perspective rendering.

McCartney (1975) presented an excellent review of former works on atmospheric optics. His work contains relevant data about the scattering phenomena under different weather conditions categorized by the heuristic parameter *atmospheric turbidity*. Since his book has been widely used in both CV and CG applications, in the present thesis we will make use of his collected information adapting it to our purpose.

In CG, Preetham *et al*. (1999) proposed a full-spectrum analytical sky model for various atmospheric conditions through turbidity. Based on this model, they developed an approximated scattering model for aerial perspective representation in complete-virtual applications. One of the issues in their work lies in the fact that his aerial perspective model cannot be directly applied to MR. Another issue is that the computational cost of implementing their model is high, thus making it no renderable in real time.

In the CV field, haze removal has been widely studied (Nayar and Narasimhan, 1999; Narasimhan and Nayar, 2002; Shwartz *et al.*, 2006; Kopf *et al.*, 2008; Tarel and Hautiere, 2009; Kristofor *et al.*, 2012). There is one representative work proposed by Narasimhan and Nayar (2003) who formulated a physics-based scattering model to solve contrast restauration issues of real scenes under uniform bad weather conditions. Their scattering model uses McCartney (1975) data and provides a faster implementation compared to Preetham *et al*. (1999).

OpenGL also offers the possibility to render virtual objects with a foggy effect in real time through its non-wavelenght dependent OpenGL Fog function (OpenGL Documentation). In order to use this function, the user has to input the color and density of the blending fog. This implementation requirement makes this method not suitable for aerial perspective rendering in MR where the density of particles in the atmosphere is difficult to estimate.

Surprisingly little work has been done on scattering modeling for MR. Recently, Zhao (2012) proposed an RGB-based aerial perspective model for MR. He estimated spectral sensitivities of various cameras and used these functions to go from spectral radiance to RGB pixel values. He employs the estimated spectral sensitivity and a simple modification of the Preetham's scattering model (Preetham *et al*., 1999) to generate an

aerial perspective effect over a virtual object inserted in a real scene. However, Zhao's straightforward adjustment of Preetham's aerial perspective model causes not so compelling synthesized appearances. Another issue in Zhao's work is that implementing his model leads to a compute-intensive task.

1.3 Proposed Approach

Aerial perspective modeling for MR depends on how similar the synthesized aerial perspective effect and the natural one are. A conventional principle of solving such problem is to find an aerial perspective model with parameters that lead to generate a realistic synthesized appearance alike the real scene. The most relevant previous works on atmospheric scattering modeling and aerial perspective rendering summed up in Table 1.2 show the advantages and disavantages of their approaches. In this thesis we propose a full-spectrum turbidity-based aerial perspective model for outdoor MR applications. For this purpose, we first estimate turbidity by matching the brightnesOurs distributions of a captured omnidirectional image and sky models. Then we use the estimated turbidity to render a virtual object with aerial perspective effect. Our rendering approach benefits from two main contributions. The first contribution is a robust and fast turbidity-estimation method. Our second contribution is our improved scattering model that uses a full-spectrum analysis, shows realistic results, and enables a fast rendering.

Table 1.2. Pros and cons of previous works compared to our thesis proposal.

	MR applicability	Rendering time	Main scattering parameter	Light spectrum utilization
Preetham et al. (1999)	No	Compute-intensive	Turbidity	Yes
Zhao (2012)	Yes	Compute-intensive	Estimated turbidity	Yes
OpenGL (fog function)	Yes	Real-time	Unknown fog's density	No
Our thesis proposal	Yes	Fast rendering	Estimated turbidity	Yes

1.4 Thesis Overview

The structure of this thesis is described as follows. Chapter 2 presents our proposed method for turbidity estimation and its evaluations. We estimated turbidity by matching the brightness distribution of an omni-directional captured image and sky models (Preetham *et al*., 1999). Chapter 3 explains our improved scattering model for MR. We employ and adapt data from McCartney (1975) to build a scattering model suitable for MR. Chapter 4 provides the rendering equation to model the aerial perspective effect and its evaluations. We first evaluatue our aerial perspective rendering model using real scenes and compare our method with results obtained using Zhao's method (2012). Then we render the Virtual Asukakyo with aerial perspective effect and compare those results with the ones obtained using Zhao's method (2012). Chapter 5 completes this thesis with summary and future work.

Chapter 2

Turbidity Estimation from Sky Image

In the previous chapter we have pointed out the importance of the turbidity in order to model the scattering coeffcicient for a specific weather condition and thus modeling the aimed aerial perspective. Therefore, an essential goal in this research is to provide a fast and robust approach for turbidity estimation that can handle a rapid implementation and can operate under different atmospheric conditions.

Zhao (2012) used an approach that calculates turbidity of a real scene with visible sky by fitting the total RGB intensity of pixels in the omni-directional captured sky image to the luminance distribution of turbidity-based Preetham sky models (Preetham *et al*., 1999). Zhao assumed a linear correlation between the relative RGB intensity at the captured image, where one pixel was taken as reference, and the relative luminance of the sky models, where the same corresponding point was taken as reference. This assumption of linear RGB intensity behavior makes his fitting-based turbidity estimation method not so robust to noises in the Preetham sky modeling. This issue occurs because the Preetham sky model presented in Equations (1.6), (1.7), and (1.8) is a non-linear luminance-based model, so using RGB intensity values in the captured image instead of *Y* luminance values will propagate the error at estimating turbidity.

In order to solve the problem found in Zhao (2012)'s turbidity estimation mehod, we propose to estimate turbidity by matching the luminance *Y* (from *XYZ* color space) of pixels in an omni-directional captured sky image and the luminance distribution of Preetham sky models. We will evaluate our proposed turbidity estimation method with domo-type and panoramic-type omni-directional images. As a mean of assessment, we will also evaluate the robustness of our turbidity estimation method when adding noise in the sun direction estimation and will compare our results with Zhao's method.

2.1 Turbidity Estimation from Omni-directional Sky Images

We estimate turbidity by matching the luminance distributions of simulated skies and an omni-directional image captured a with fish-eye lens camera. As for the simulated skies, we use the Preetham sky model due to its simplicity instead of other sky models (Nishita *et al.*, 1993; Nishita *et al.*, 1996; Haber *et al.*, 2005; Habel *et al.*, 2008; Elek and Kmoch, 2010; Hosek and Wilkie, 2012) that might generate better sky apperances than Preetham's but spend high computational cost or need pre-set data.

Figure 2.1 illustrates the basic idea of the proposed turbidity estimation approach. First, we estimate the sun position at the captured image by finding the center of the elipse that fits the saturated area where the sun lies. This estimated sun direction is important since it will be applied to the Preetham sky model used as sky models for this thesis. Then we assume a linear relation between the relative (sampling point "*i*" to reference point "*ref*") luminance $Y_i(T)/Y_{ref}(T)$ in the Preetham sky model and the corresponding relative luminance Y_i/Y_{ref} in the captured image. We can obtain the ratio $Y_i(T)/Y_{ref}(T)$ from the Preetham sky model shown in Equation (1.6) and the ratio Y_i/Y_{ref} from the Y-channel of the XYZ color space. Afterwards, we estimate the turbidity by

$$\arg\min_{T\in[1,20]} \sum_{i=1}^{N} \left| \frac{Y_i(T)}{Y_{ref}(T)} - \frac{Y_i}{Y_{ref}} \right|, \tag{2.1}$$

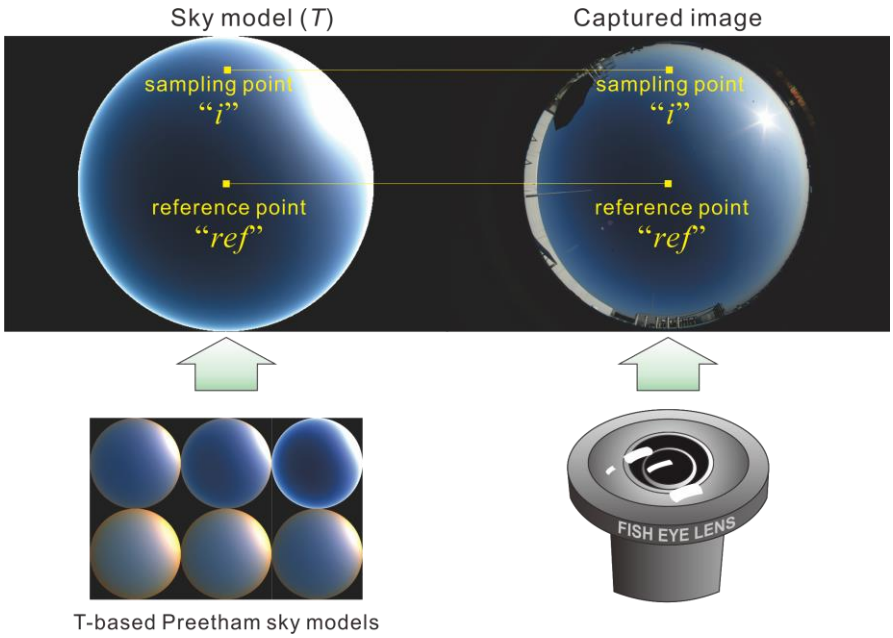

Figure 2.1. Turbidity estimation by comparing sky models and an omni-directional sky image captured by fish-eye lenses.

where N is the number of sample points used in the calculation process, the refrence point *ref* can be either the zenith or any other point in the visible sky portion, and the turbidity rangs from 1 to 20.

In orther to solve Equation (2.1), we use the Levenberg-Marquardt algorithm (LMA) also known as Damped Least-Squares (DLS) method, which is generally used in mathematics and computing for solving the problem of minimizing a function.

Since the Preetham sky model does not handle clouds, we will use the same Random Sample Consensus (RANSAC) approach for cloudy skies used by Zhao (2012). Basically, the RANSAC method arbitrarily chooses a fraction of the N sampling points commonly used in clear skies, assumes them as inliers, and estimates turbidity. If the estimated turbidity is too high, there is a great chance that most of the inliers are cloudy pixels, so we use the estimated turbidity to test the other sampling points. Here we calculate the *Err* corresponding to one sampling point and put it into the hypothetical inlier set if *Err* is smaller than the threshold. Then turbidity is estimated from the new inlier set, and we calculate *Err*. This process is reiterated until completing the N sampling points. Finally, we estimate turbidity from the inlier set with the smallest *Err*.

Our turbidity estimation approach does not depend either on the camera sensitivity or white-balance setting and uses a similar general idea as Zhao (2012), however, differs in three aspects. First, we use random sampling points instead of uniform distributed patches in the sky. Second, we employ LMA for the error minimization instead of the Particle Swarm Optimization. The last difference is that we use the Y-channel from XYZ color space for analyzing the luminance in the captured image instead of the total RGB intensity of a pixel used by Zhao. Especially the last difference makes our turbidity estimation method a more robust approach to errors in sun position estimation, which we will show in the following section.

2.2 Turbidity Estimation Approach Evaluation

2.2.1 Evaluation with Sky Models

We tested the proposed method for turbidity estimation when input images were simulations of the Preetham sky model. For this purpose we implemented the Preetham sky models, which are illustrated in Figure 2.2. These models are sky images of 500 by 500 pixels with different values of turbidity ranging from 2.0 to 9.0 and sun position: θ_s=58.4

degrees, ϕ_s=-179.4 degrees. N=100 random sampling points were taken for each turbidity estimation. Turbidity was estimated 100 times. Then the sky models were tested by the proposed turbidity estimation method and the results are shown in Table 2.1. From here, T_{mean} stands for the mean value of turbidity and T_σ stands for its corresponding standard deviation. The speed of the proposed turbidity estimation method was 200 sampling points/sec.

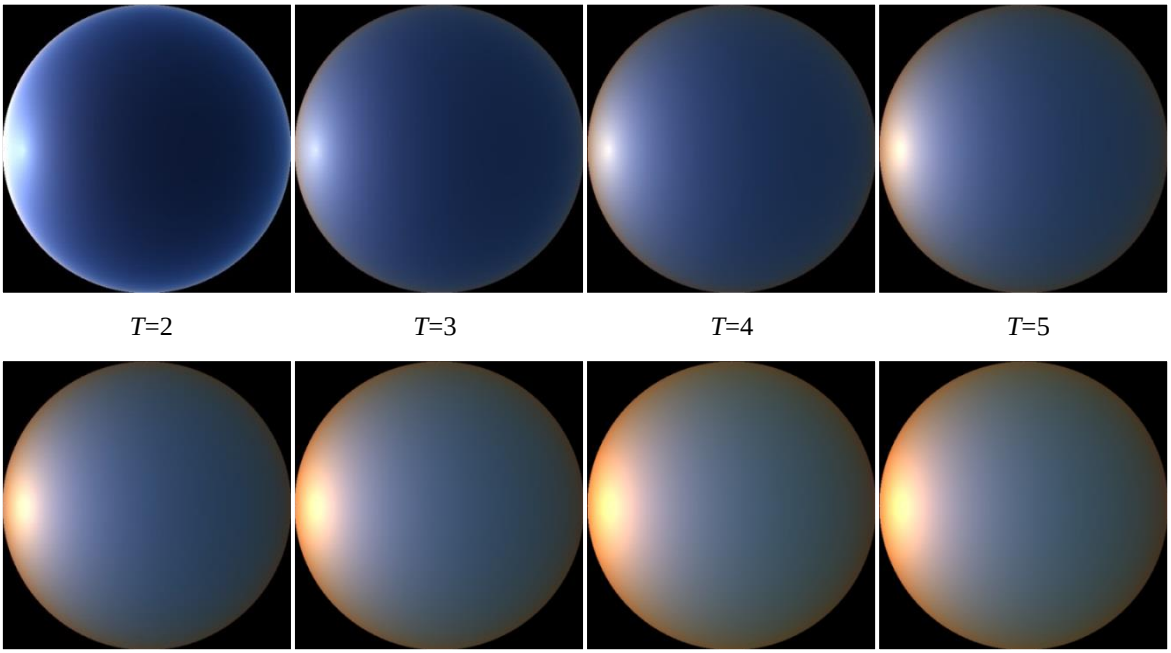

Figure 2.2. Implemented Preetham sky models for turbidities ranging from 2 to 9.

Table 2.1. Estimated turbidity values using the Preetham sky models as an input image.

$T_{sky\ model}$	T_{mean}	T_σ
2.0	2.011791	0.004660
3.0	2.851666	0.027230
4.0	4.241544	0.043840
5.0	4.992700	0.055292
6.0	5.836839	0.061853
7.0	7.138090	0.062630
8.0	8.010996	0.135764
9.0	9.099154	0.089461

Robustness in the sun direction: When we match an omni-directional captured sky image with Preetham sky models, we first estimate the sun position at the captured image by calculating the center of the elipse that fits the saturated area where the sun lies. This error at the sun position estimation propagates the error to the Phreetham sky model of Equation (1.6) and Equation (1.7) by

$$\frac{\partial\left(\frac{Y_V}{Y_z}\right)}{\left(\frac{Y_V}{Y_z}\right)} = \frac{\partial\theta_s}{\theta_s}\left(\frac{E\theta_s \sin 2\theta_s - CD\theta_s e^{D\theta_s}}{1+Ce^{D\theta_s}+E\cos^2\theta_s}\right), \tag{2.2}$$

where the expression on the left side is the relative error of Y_V/Y_z at the Preetham sky model, and the expression on the right side is the relative error of θ_s (estimated sun position) multiplied by a non-linear factor that depends on the estimated sun position and the distribution coefficients of Perez *et al*. (1993) shown in Equation (1.8).

In order to evaluate how much the error at sun direction estimation in the captured image affecs the turbidity estimation, we analyze the case where the captured image is a simulated sky with known sun direction. The sky model with T=2.0 was tested by the proposed turbidity estimation method adding errors to the sun direction estimation, and the results are shown in Figure 2.3. For the computation, N=100 random sampling points were taken per turbidity estimation and turbidity was estimated 60 times. The proposed method was compared with Zhao (2012)'s turbidity estimation approach and proved to obtain better results.

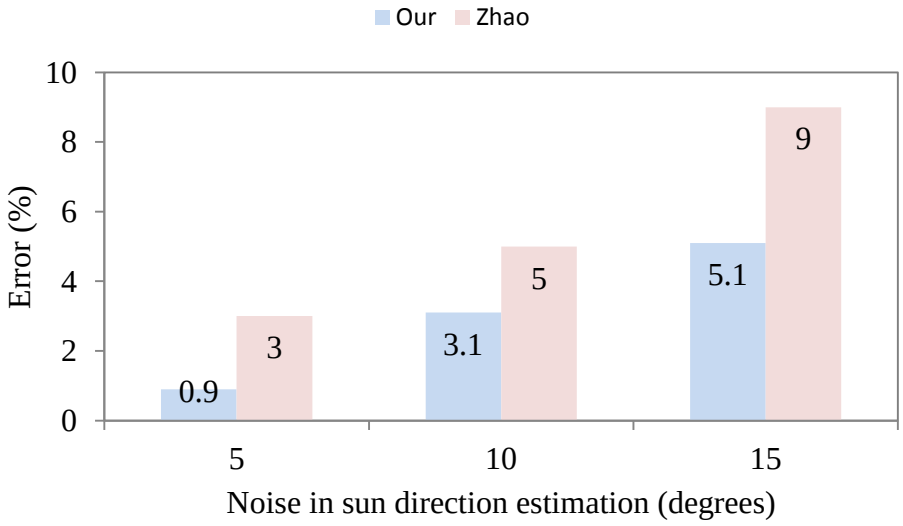

Figure 2.3. Turbidity estimation robustness when adding noise in the sun direction estimation.

The reason why adding errors to the sun position estimation propagates more in the case of Zhao's turbidity estimation method than in our approach lies in Zhao's relative luminace model at the captured image. Zhao uses the total intensity values (summation of intensities of RGB channels) at pixels in the captured image for evaluating the relative luminance of Equation (2.1), while we employ the Y-luminance (from XYZ color space) according to The Preetham sky model which utilizes a Y-based Equation (1.8) to model the five distribution coefficients Perez *et al*. (1993) via turbidity. We have proved that adding error to the distribution coefficients will propagate the error in the Phreetham sky model according to Equation (2.2), thus resulting in an error propagation of the turbidity estimation approach which uses the Preetham sky model.

2.2.2 Evaluation with Real Scenes

We also tested the turbidity estimation approach when the input images where captured by camera. Here we show the results obtained when applying the proposed method to two different types of omnidirectional images: sky-dome omni-directional images and panoramic omni-directional images.

Evaluation with sky-dome omni-directional images: The first image shown in Figure 2.4 is a 4368 by 2912 pixel image taken by Canon EOS5D with fisheye lens. At first, the camera view direction respect to the sun was calibrated so that the optical axis of the camera was perpendicular to the ground. The sun direction was estimated by extracting the saturated area of the image and then fitting it as an ellipse. Then the sun direction was calculated as the center of the extracted ellipse: θ_s=54.5 degrees, ϕ_s=-33.5 degrees. Afterwards, N=100 random sampling points were taken per turbidity estimation and turbidity was estimated 50 times. The obtained results were T_{mean}=1.835959 and T_{σ}=0.005583. Figure 2.4 shows also the corresponding sky model for the same sun direction and T=1.83; we can notice a compelling synthesized appearance of the simulated sky according t the real captured sky.

Analyzing Figure 2.4, we also evaluated the correlation between the luminance of the captured image and the luminance of the sky model in the N sampling points used for the turbidty estimation. The result of this evaluation is provided in Figure 2.5 and proves to be almost linear, thus leading to the conclusion that our turbidty estimation method found

the most suitable matching. Furthermore, in orther to evaluate the flexibility of our turbidity estimation method, we estimated turbidities for skies under several atmospheric conditions and show our results in Figure 2.6.

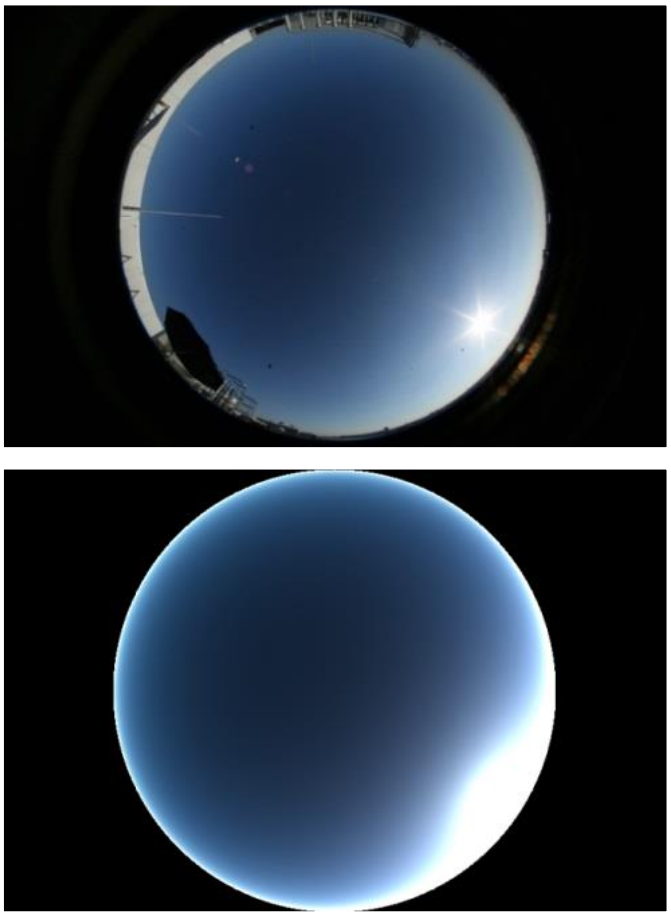

Figure 2.4. Turbidity estimation for dome-type omnidirectional sky image. Image on the top was captured by Canon EOS 5D. Image on the bottom is its corresponding sky model.

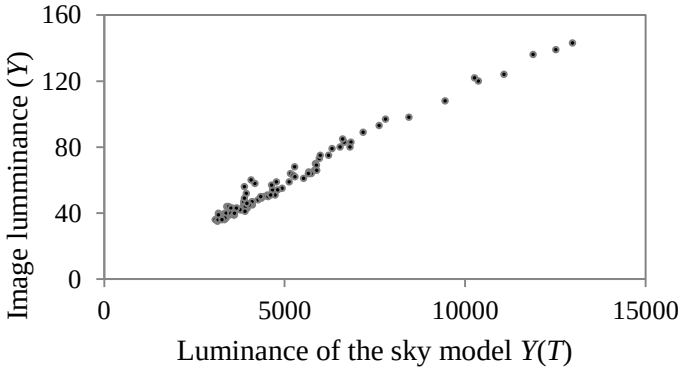

Figure 2.5. Correlation between luminance of the captured image and luminance of its corresponding sky model.

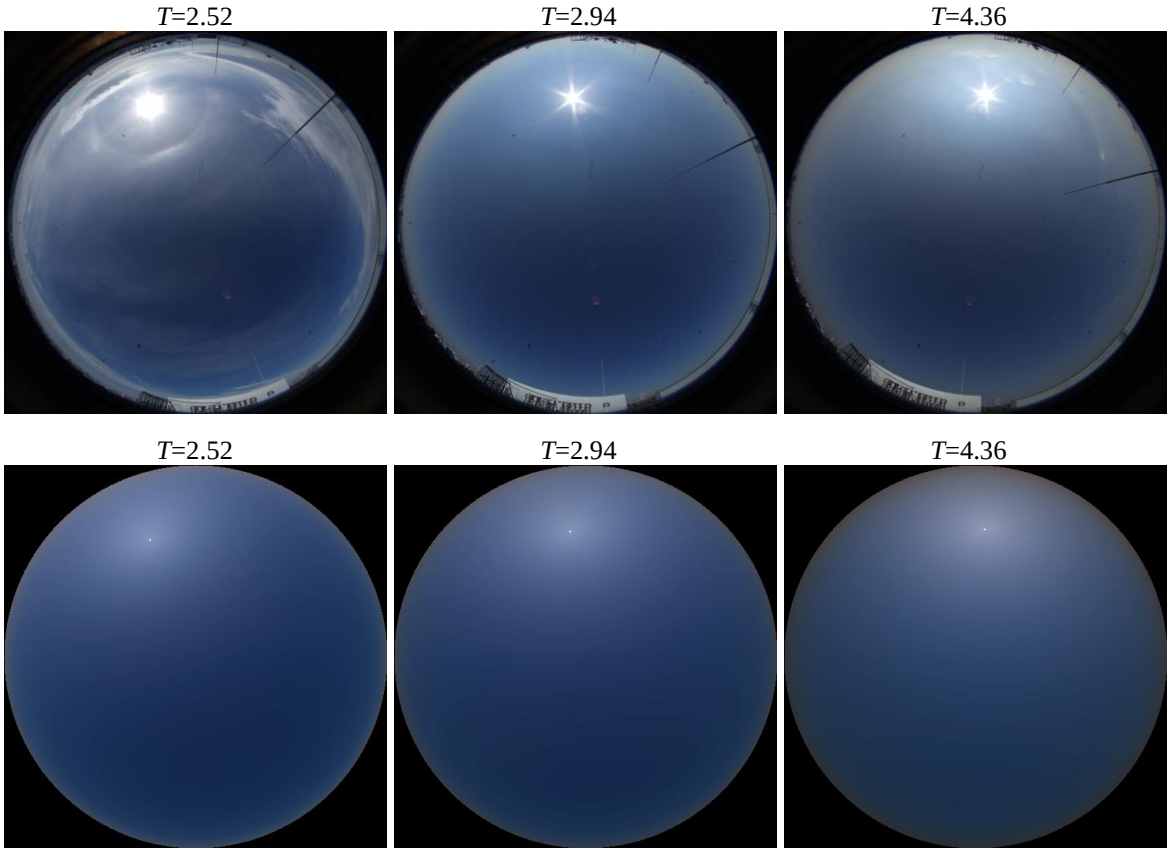

Figure 2.6. Turbidity estimation results. (Top) Pictures by Canon EOS5D with fisheye lens. (Bottom) Corresponding simulated skies for turbidities.

Evaluation with panoramic omni-directional images: The image illustrated in Figure 2.6 is a 5400 by 2700 pixel image taken by the spherical vision camera Ladybug2 by Point Grey Research Inc. In this image, the sun direction was calculated from the longitude, latitude, and time: θ_s=42.1 degrees, ϕ_s=356.3 degrees. We used this method for sun direction estimation, instead of analyzing the saturated pixels in the sky like in the previous case, since the sun was covered by clouds. Afterwards, N=500 random sampling points in the visible portion of the sky were taken per turbidity estimation and turbidity was estimated 50 times. The obtained results were and T_{mean}=1.877058 and T_{σ}=0.0215. Figure 2.7 also shows the corresponding sky model for the same sun direction and turbidity value T=1.87. Besides, we analyze the N sampling points used for the turbidity estimation and found the correlation between the intensity of the captured image and the luminance of the sky model, which is shown in Figure 2.8. Figure 2.8 shows a less linear response than Figure 2.5; this is caused by the cloudy pixels present in Figure 2.7.

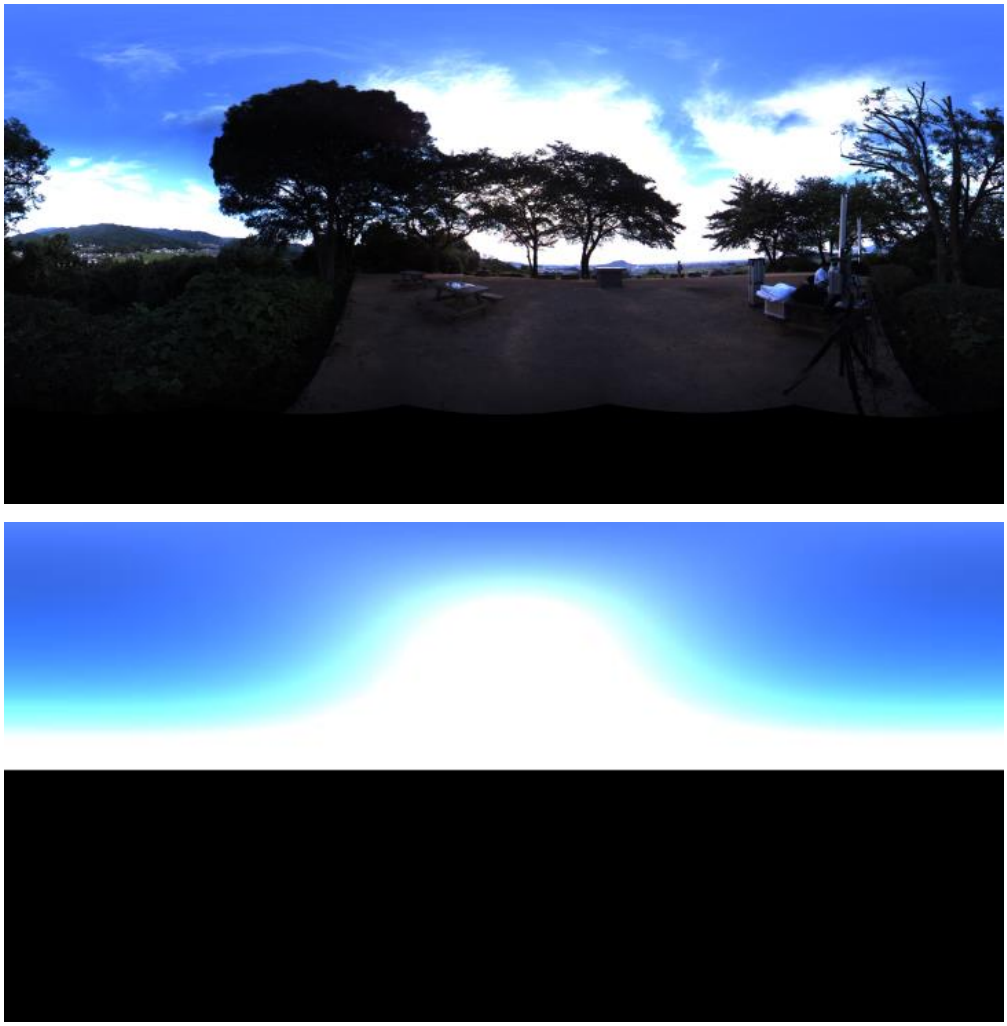

Figure 2.7. Turbidity estimation for panoramic-type omnidirectional sky image. Image on the top was captured by Ladybug2. Image on the bottom is its corresponding sky model.

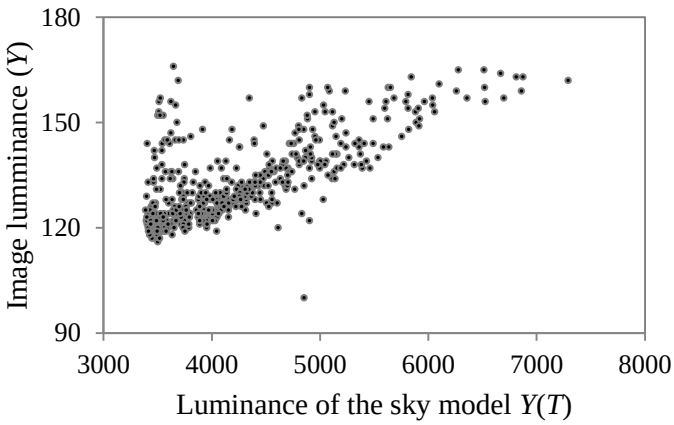

Figure 2.8. Correlation between luminance of the captured image and luminance of its corresponding sky model.

2.3 Summary

We have presented a turbidity estimation method that is based on matching the luminance distributions of Preetham sky models and a captured image taken under various weather conditions. Our proposed method does not depend either on the camera's sensitivity or white-balance settings. We have evaluated our turbidity estimation method with both simulated skies and real omni-directional sky images (domo type and panoramic type), and the results show great accuracy under different weather conditions. Another important contribution is that our proposed turbidity estimation method is more robust to errors at sun position estimation than Zhao (2012)'s turbidity estimation approach.

Chapter 3

Aerial Perspective Rendering in MR

Rendering virtual objects with aerial perspective effect is essensial for increasing realism in outdoor MR where the observer is far from the target (Goldstein, 1980). Currently there is only one research proposed by Zhao (2012) that handles aerial perspective rendering for MR. He calculated spectral sensitivities of several cameras and used their values to go from spectral radiance to RGB. Zhao combined the spectral sensitivity of a camera with a straightforward correction of Preetham's turbidity-based aerial perspective model to render a virtual object with aerial perspective effect under a clear atmospheric condition (low turbidity value). However, he did not analyzed how his synthesized aerial perspective effect varies as the atmospheric condition changes (higher turbidities). Besides, another issue in his work is that the computational cost is high, thus making his aerial perspective effect not renderable in real time.

In this chapter, we formulate and evaluate a turbidity-based aerial perspective rendering model for MR. First, we formulate an improved scattering model for MR applications based on McCartney (1975) and adapt his data to provide a classification of scattering coefficients through turbidity. We adapt Rayleigh and Mie scattering coefficient models described in Chapter 1 to their corresponding values obtained through experimentation in McCartney (1975). Then we use our improved scattering models under various weather conditions to categorize scattering coefficients via turbidity. To formulate our aerial perspective rendering equation, we benefit from Zhao (2012)'s spectral sensitivities to go from spectral radiance to RGB values. We evaluate the realism of the appearance generated by our synthesized aerial perspective effect compared to Zhao's aerial perspective model through the utilization of natural atmospheric effects observed in real scenes under different weather conditions.

3.1 Improved Scattering Model for MR

In this subsection, we formulate corrections of both Rayleigh and Mie scattering coefficients to make them applicable to MR. To do so, we base our analysis on McCartney (1975)'s conmpilation of previous works on scattering phenomena modeling.

3.1.1 Rayleigh Scattering Coefficient Correction

We need to adjust the Rayleigh scattering coefficient to make it suitable for outdoor MR. For this purpose, we adapted data from McCarteny (1975) that relates weather conditions via scattering coefficients and summarize it in Table 3.1. Using Table 3.1 we can obtain the value of the Rayleigh scattering coefficient of β_R=0.0141 Km^{-1} for a spectrally weighted average wavelength (550 nm). However, using Equation (1.3) for λ=550 nm and h=0 m (standard conditions), we obtain β_R=0.0135 Km^{-1}. Therefore, we propose a straightforward multiplicative correction factor K_R given by

$$K_R = \frac{0.0141}{0.0135} = 1.0396. \tag{3.1}$$

Then our modified Rayleigh scattering coefficient is given by

$$\beta_R = \frac{8\pi^3 (n^2 - 1)^2}{3N\lambda^4} \left(\frac{6 + 3p_n}{6 - 7p_n} \right) K_R \times e^{\frac{-h_0}{H_0}}, \tag{3.2}$$

where n, p_n, H_0, and N are same as in Equation (1.3), h_0 is the height at the observer, and K_R is given by Equation (3.1).

Table 3.1. Weather conditions via scattering coefficients for spectrally weighted average wavelength (550 nm). Adapted from McCarteny (1975)

Condition	β_M	Min β_R (Km^{-1})	Max β_R (Km^{-1})
Pure air	0.0141	0	0
Exceptionally clear	0.0141	0.0639	0.0639
Very clear	0.0141	0.0639	0.1819
Clear	0.0141	0.1819	0.3769
Light haze	0.0141	0.3769	0.9399
Haze	0.0141	0.9399	1.9459
Fog	0.0141	1.9459	More than 78

3.1.2 Mie Scattering Coefficient Correction

One issue in Preetham's scattering model (1999) is related to the turbidity itself. From the definition of turbidity in Equation (1.5), T=1 refers to the ideal case where the Mie scattering coefficient is cero. That is, the turbidity-dependent concentration factor c in Equation (1.4) should be cero for T=1. More specifically, Preetham (1999) used a concentration factor of $c=(0.6544T-0.6510)\times10^{-16}$, while Zhao employed a corrected $c=(0.6544T-0.6510)\times10^{-18}$ for MR. We observe that Zhao's concentration factor is 100 times smaller than Preetham's concentration factor. In fact, Zhao applied that correction to compensate the strong attenuation effect that Preetham's concentration factor has when it is applied to MR. However, by simple inspection we can deduce that both concentration factors are not cero for T=1. Hence, we propose a concentration factor which is a modification of Preetham's concentration factor and is given by

$$c(T) = (0.65T - 0.65)\cdot 10^{-16}. \tag{3.3}$$

Another important issue is the value of the Fudge factor K used by Preetham (1999) and Zhao (2012). They utilized a wavelength-dependent K whose value varies between 0.65 and 0.69 for wavelengths ranging from 380 to 780nm. In fact, we can deduce this Fudge factor from McCartney (1975). Preetham considered a turbidity of 1.6 for an exceptionally clear weather condition. We will use that assumption since we will also employ the Preetham sky model that depends on turbidity. From Table 3.1, an exceptionally clear condition is categorized by a Mie scattering coefficient of 0.0639Km^{-1}. Therefore, we can solve Equation (1.4) under standard conditions (λ=550nm and h=0m) and calculate a corrected Fudge factor under such conditions. Then we propose the following non-wavelenght dependent Fudge factor:

$$K_M = 0.0092. \tag{3.4}$$

Finally, our modified Mie scattering coefficient can be written as

$$\beta_M = 0.434c(T)\pi\left(\frac{2\pi}{\lambda}\right)^{\nu-2} K_M \times e^{\frac{-h_0}{H_0}}, \tag{3.5}$$

where c is given by Equation (3.3), K_M is given by Equation (3.4), and υ, h_0, and H_0 are same as in Equation (1.4).

From both corrections in the concentration factor and the Fudge factor that we propose, we can observe that, under standard conditions (λ=550nm and h=0m), our proposed Mie scattering coefficient is approximately 70 times smaller than the Mie

scattering coefficient used by Preetham *et al*. (1999) and roughly 1.43 times smaller than the corrected Mie scattering coefficient employed by Zhao (2012) for MR applications. In fact, if we focus on the the effect caused by the Mie scattering coefficient, we can approximate Preetham's attenuation factor as $Att_{Preetham} = e^{-\beta_{sc}.s}$, Zhao's corrected attenuation factor as $Att_{Zhao} = e^{-0.01\beta_{sc}.s}$, and our attenuation factor as $Att_{Our} = e^{-0.0137\beta_{sc}.s}$. Therefore, using these approximated attenuation factors, we can plot a rough relation between the attenuation factor obtained using Preetham's, Zhao's, and our proposed scattering model (see Figure 3.1). It is well noted from Figure 3.1 that Preetham's attenuation factor is smaller than ours, thus making a stronger attenuation. Conversely, Zhao's attenuation factor is bigger than ours, thus causing a weaker attenuation.

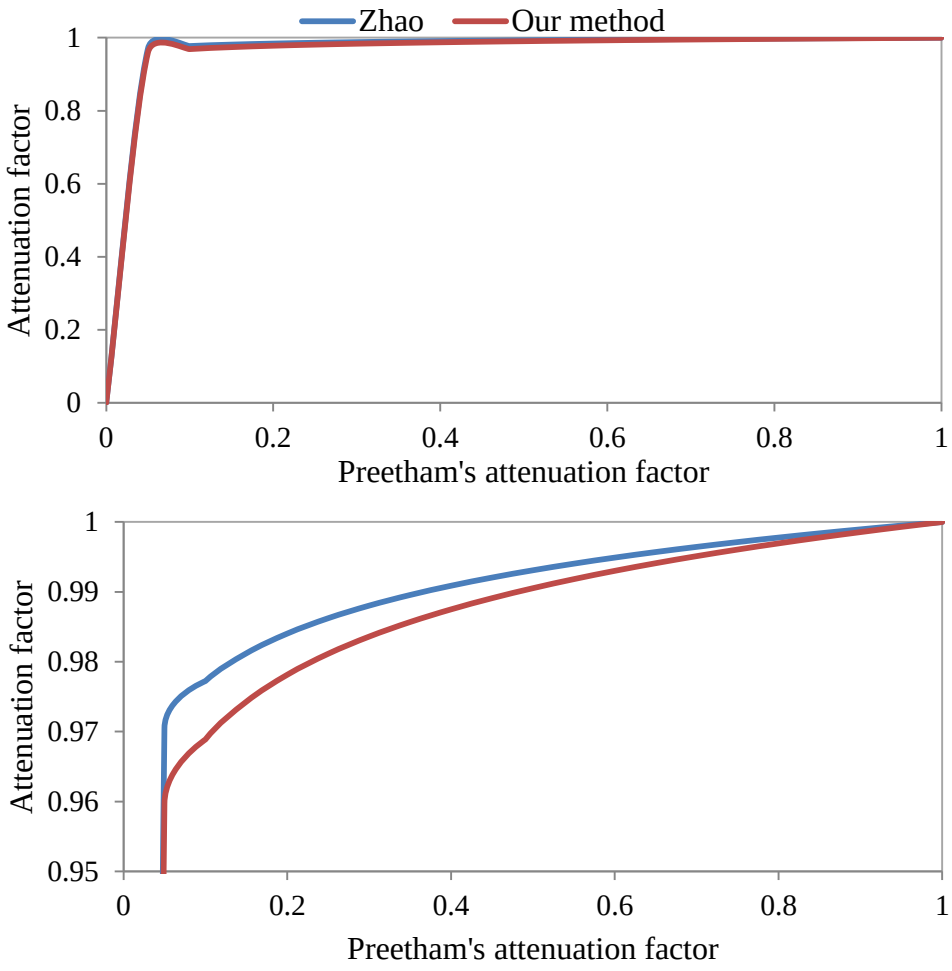

Figure 3.1. Approximate relation between the attenuation factor of Preetham *et al*. (1999), Zhao (2012), and our proposal. Image on the top shows the comparison in a full scope. Image on the bottom highlights a small scope area.

3.2 Scattering Coefficient via Turbidity

We provide a classification of scattering coefficients via turbidity using Table 3.1 and our improved Rayleigh and Mie scattering coefficients. Based on Equations (3.2) and (3.5) we obtain the following relation between Mie scattering coefficients under different weather conditions via turbidity:

$$\frac{\beta_{M1}}{\beta_{M2}} = \frac{T_1 - 1}{T_2 - 1}, \tag{3.6}$$

where β_{M1} and β_{M2} are our improved Mie scattering coeeficients for turbidities T_1 and T_2.

Simmilarly than Preetham *et al*. (1999), we also consider a turbidity of 1.6 for the case of an exceptionally clear atmospheric condition. Using this assumption and Table 3.1, we can say that T_1=1.6 corresponds to β_{M1}=0.0639 and, likewise, we can state that T_2 corresponds to β_{M2}=0.1819, which is the lower bound where a clear atmospheric condition strats. Therefore, using Equation (3.6), we can calculate the turbidity T_2=2.7. We repeat this process and build Fugure 3.2, which is a graph that categorizes scattering coefficients under different weather conditions via turbidity.

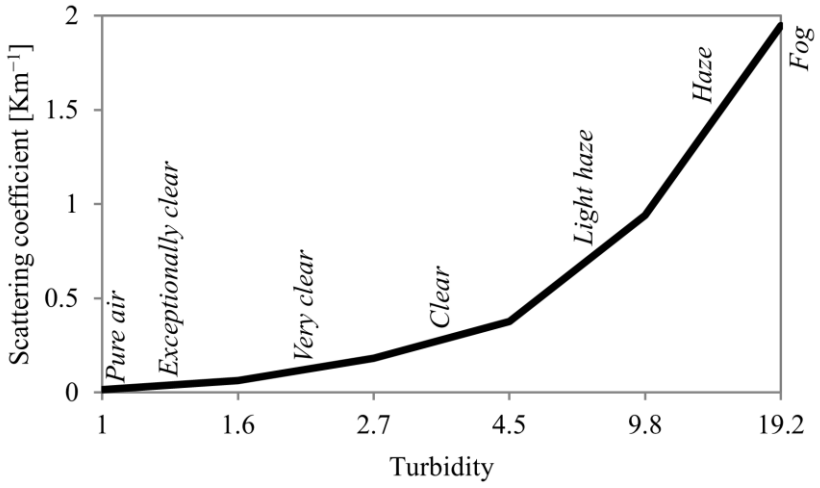

Figure 3.2. Scattering coefficients through turbidity.

3.3 Aerial Perspective Rendering Model for MR

We propose an aerial perspective rendering model for MR that is based on the general outdoor illumination model shown in Figure 3.3, our improved turbidity-based scattering model for MR, and the spectral sensitivities calculated by Zhao (2012) and introduced in Chapter 1. Figure 3.3 illustrates an outdoor scenario where an observer is watching a target

at distance *s*. There the total light perceived by the observer is a summation of two components: the *direct transmission*, which stands for the remaining light obtained from the target's light that is attenuated until it reachs the observer, and the *airlight*, which is the light obtained from the environmental illumination that is scattered in the same path as the viewing direction and then attenuated in its way to the observer.

From the general aerial perspective model detailed in Equation (1.9) and the rendering equation shown in Equation (1.10) we can deduce that the camera used by the observer in Figure 4.1 records the intensity value I_c of a target object's pixel at distance s for the channel c∈{r,g,b} as

$$I_c(s) = \int_{380\text{nm}}^{780\text{nm}} L(0,\lambda)e^{-\beta_{sc}(\lambda,T,h_0)s}q_c(\lambda)d\lambda + \int_{380\text{nm}}^{780\text{nm}} L(\infty,\lambda)(1-e^{-\beta_{sc}(\lambda,T,h_0)s})q_c(\lambda)d\lambda\,, \qquad (3.7)$$

where the light $L(0,\lambda)$ coming from the target, the environmental illumination $L(\infty,\lambda)$, and the distance s observer-target are same as in Equation (1.9). Besides, the height h_0 at the observer from sea level and the total scattering coefficient $\beta_{sc}=\beta_R+\beta_M$ are same as in Equations (3.2) and (3.5).

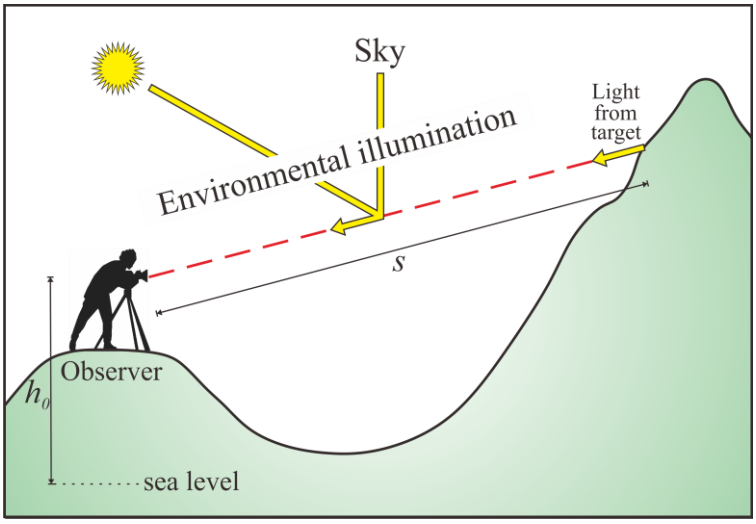

Figure 3.3. Basic illumination model for outdoor scenarios.

To solve Equation (3.7) we need to estimate the following six parameters: β_{sc}, $L(\infty,\lambda)$, $L(0,\lambda)$, q_c, h_0, and s. While the later three parameters can be obtained from the settings of the MR system itself, the first three parameters need special attention.

Regarding to β_{sc}, we handle it by first estimating turbidity through our proposed turbidity estimation method explained in Chapter and then using our improved scattering model described in Equations (3.2) and (3.5).

Concering to $L(\infty,\lambda)$, we cannot directly estimate $L(0,\lambda)$ when the target is a virtual object as we don't know the object's reflectance properties. However, assuming that the virtual object is captured by the camera, we can approximate the intensity of the light coming from the object using Equation (1.10). Besides, approximating the camera's sensitivity by a Dirac delta function, we can rewrite Equation (3.7) as

$$\text{Direct transmission} = \left(\int_{380\text{nm}}^{780\text{nm}} L(0,\lambda) q_c(\lambda) d\lambda \right) \left(\frac{\int_{380\text{nm}}^{780\text{nm}} e^{-\beta_{sc}(\lambda,T,h_0)s} q_c(\lambda) d\lambda}{\int_{380\text{nm}}^{780\text{nm}} q_c(\lambda) d\lambda} \right), \tag{3.8}$$

where the first term in brackets is the recorded intensity value of a pixel at the virtual object's surface and the second term is a non-wavelenght dependent factor that we will call *weighted attenuation factor* and represent by

$$\Gamma_c(T,s,h_0) = \frac{\int_{380\text{nm}}^{780\text{nm}} e^{-\beta_{sc}(\lambda,T,h_0)s} q_c(\lambda) d\lambda}{\int_{380\text{nm}}^{780\text{nm}} q_c(\lambda) d\lambda}. \tag{3.9}$$

As to the environmental illumination, we will apply an approach different than the ones proposed by Preetham *et al*. (1999) and Zhao (2012). Preetham *et al*. formulated a turbidity-dependent model of the spectral radiance of the sun and skylight; however, their model proves to have mainly two disadvantages. First, Preetham *et al*.'s environmental illumination model has a high computational cost, thus making its utilization not suitable for applications that require fast rendering. Second, we cannot convert Preetham's spectral radiance of sun and skylight to RGB values. Zhao tried to solve that RGB-conversion issue by using a multiplicative factor of $8.32\text{x}10^{-12}$ applied to the total spectral radiance of the sun and skylight. That multiplicative factor makes the highest Sun spectral radiance (30663.7 $\text{Wm}^{-2}\text{nm}^{-1}\text{sr}^{-1}$ for λ=480 nm according to Wyszecki and Stiles, 1982) equal 255 in RGB value. Zhao was able to render an aerial perspective effect for MR using that assumption, however, only implemented one atmospheric case with T=1.8, thus not being

able to prove the generalization of his method. We will show that Zhao's aerial perspective fails since it generates strong dark appearances for various atmospheric conditions. Due to these drawbacks, we propose to estimate $L(\infty,\lambda)$ from the sky pixels in the image captured by the camera. Assuming that the environmental illumination is globally constant in daylight applications and that the camera's spectral sensitivity can be approximated by a Dirac delta function, we can rewrite the airlight component of Equation (3.7) as

$$\text{Airlight} = \left(\int_{380\text{nm}}^{780\text{nm}} L(\infty,\lambda) q_c(\lambda) d\lambda \right) \left(1 - \frac{\int_{380\text{nm}}^{780\text{nm}} e^{-\beta_{sc}(\lambda,T,h_0)s} q_c(\lambda) d\lambda}{\int_{380\text{nm}}^{780\text{nm}} q_c(\lambda) d\lambda} \right), \tag{3.10}$$

where the first term in brackets stands for the intensity of the environmental illumination and the second term is one minus the weighted attenuation factor of Equation (3.9).

Finally, using our assumpions regarding β_{sc}, $L(0,\lambda)$, and $L(\infty,\lambda)$ and employing Equation (4.1), we propose the turbidity-based aerial perspective rendering equation as

$$I_c(T,s,h_0) = I_{0,c} \cdot \Gamma_c(T,s,h_0) + I_{\infty,c}(1 - \Gamma_c(T,s,h_0)), \tag{3.11}$$

where $I_{0,c}$ is the intensity of the light coming from the virtual object and is given by the $c \in \{r,g,b\}$ value of a pixel at the object's surface, $I_{\infty,c}$ is the intensity of the environmental illumination at infinite point and is given by the highest $c \in \{r,g,b\}$ value of the pixel near the horizon in the input image, and Γ_c is the weighted attenuation factor of Equation (3.9).

3.4 Aerial Perspective Rendering Evaluation with Real Scenes

In order to compare our synthesized aerial perspective effect with the natural atmospheric effect, we evaluated our rendering model with real images under different weather conitions. We implemented two kinds of evaluations based on single real scenes in the first case and two real scenes in the second case. For a fair comparison we performed all of the evaluations under same illumination conditions (same camera settings and same time for capturing images at different days).

3.4.1 Evaluation from Single Real Scenes

The natural aerial perspective phenomenon over real scenes is modeled as a summation of the direct transmission and airlight. In this subsection we compare those components using

our aerial perspective rendering model and Zhao (2012)'s aerial perspective model. For this purpose, we first extract the airlight constitutent of a captured image and then calculate the direct transmission by subtraction. Figure 3.4 illustrates the scheme of an outdoor scene being split in those components and allows us to emphasize two aspects. First, airlight should only contain color information of environmental illumination. Second, direct transmission contains color information of target objects depending of their reflectance properties. In Figure 3.4, the targeted mountains in the direct transmission only contain colors of trees and ground; however, different would be the case if the target is a mirror. We also notice a darkening effect due to attenuation on direct transmission and airlight.

We estimated the direct transmission and airlight constituents of real images captured by Canon EOS 5D using our rendering model of Equation (3.11). First we estimated turbidity in those scenes capturing the sky with fish-eye lens and applying our estimation method proposed in Chapter 2. Then we captured a target scene using zoom lens, as illustrated in Figure 3.5, Figure 3.6, and Figure 3.7. Those figures also illustrate the results obtained using our aerial perspective rendering model and Zhao (2012)'s model. From those figures, we notice the following three aspects. First, as the turbidity increases, we observe that the contrast between our airlights on the mountains (50-100km away) and the environmental illumination color near the horizon decreases, while the contrast in Zhao's case increases. Second, our airlight tends to keep the environmental illumination color, while Zhao's airlight does not. Last, as the turbidity increases, our direct transmission causes a stronger darkening effect over the distant mountains, while Zhao's direct transmission makes a brightening effect. To sum up, those three aspects in Zhao's case contradict logics.

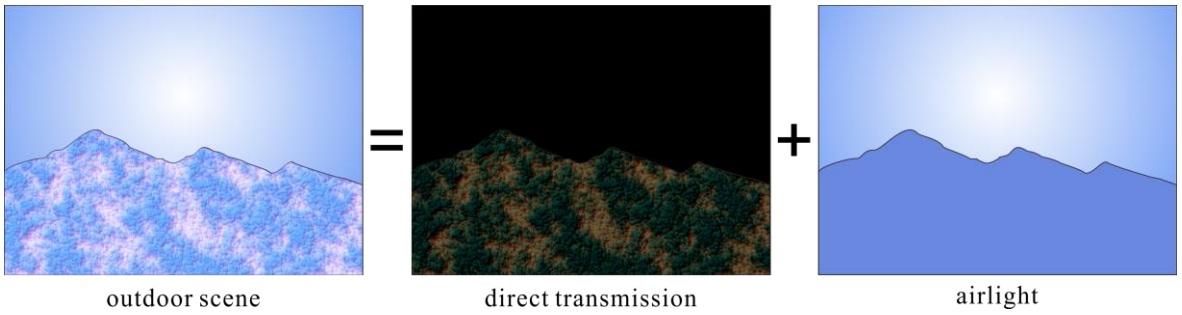

Figure 3.4. Scheme of outdoor scene divided in its aerial perspective componets (direct transmission and airlight).

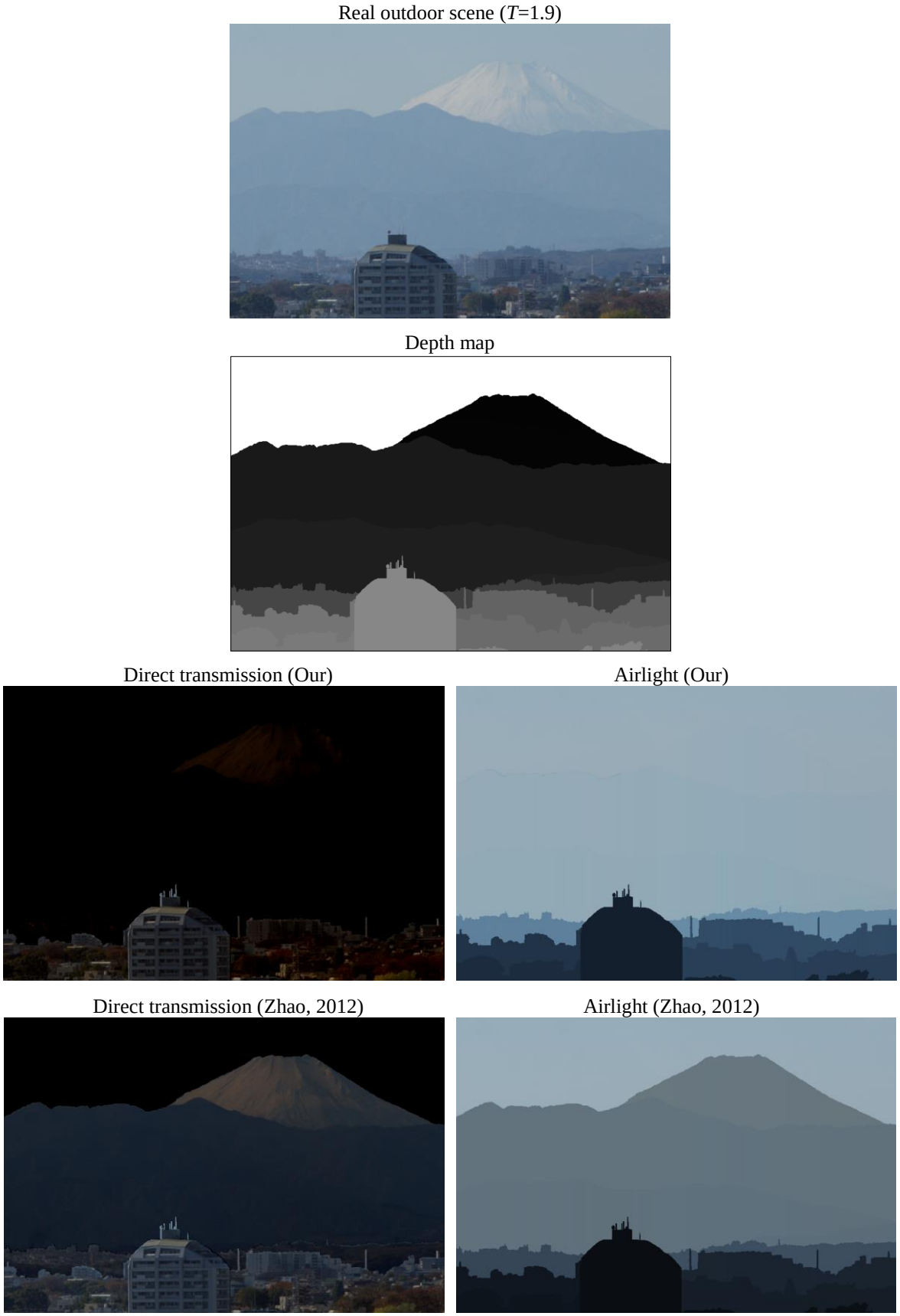

Figure 3.5. Outdoor scene of T=1.9 (with its depth map from Google earth) divided in its direct transmission and airlight using our method and Zhao (2012)'s method.

Real outdoor scene (*T*=2.94)

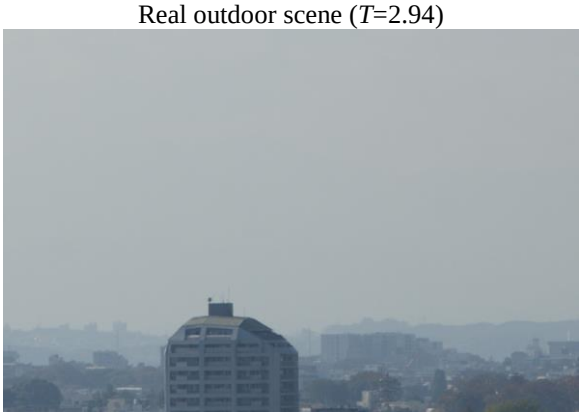

Depth map

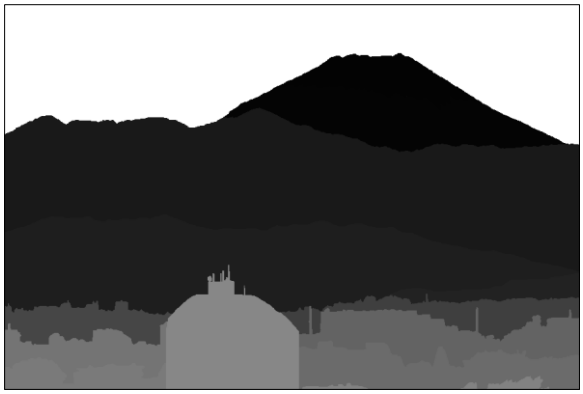

Direct transmission (Our)

Airlight (Our)

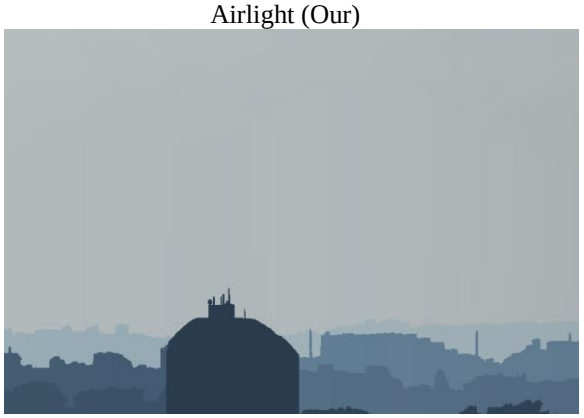

Direct transmission (Zhao, 2012)

Airlight (Zhao, 2012)

Figure 3.6. Outdoor scene of *T*=2.94 (with its depth map from Google earth) divided in its direct transmission and airlight using our method and Zhao (2012)'s method.

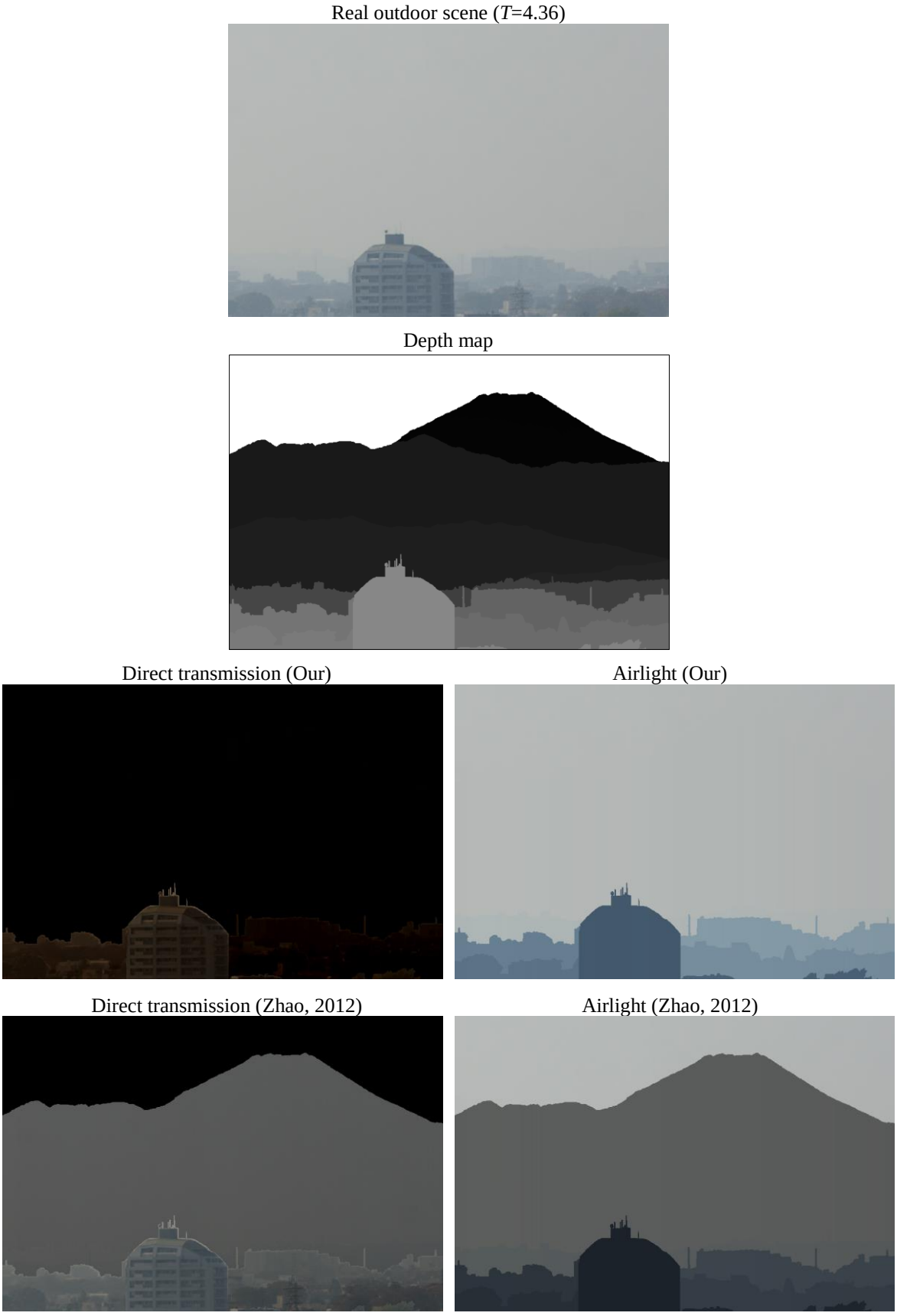

Figure 3.7. Outdoor scene of T=4.36 (with its depth map from Google earth) divided in its direct transmission and airlight using our method and Zhao (2012)'s method.

3.4.2 Evaluation from Two Real Scenes

Figure 3.8 illustrates the scheme used for analyzing two real scenes, “scene1” and “scene 2”, under different atmospheric conditions. Based on that scheme, if we assume constant reflectance properties under different weather conditions for the same object in “scene 1” that appears in “scene 2”, we can obtain the following from Equation 3.11:

$$\frac{I_c^{(1)}(s)}{I_{\infty,c}^{(1)}(s)} = \frac{I_c^{(2)}(s)}{I_{\infty,c}^{(2)}(s)}, \tag{3.12}$$

where the upper indexes $^{(1)}$ and $^{(2)}$ correspond to features in “scene1” and “scene 2” and s stands for the distance of the object from the observer

Then using Equation (3.12) in Equation (3.11), we can formulate a new aerial perspective rendering model that uses features of “scene 1” and “scene 2” to render an aerial perspective similar to the natural atmospheric phenomena of “scene 2” by

$$I_c^{(2)\mathrm{AP}}(s) = I_c^{(1)}(s)\left[\frac{I_{\infty,c}^{(2)}}{I_{\infty,c}^{(1)}}\frac{\Gamma_c^{(2)}(T_2,s)}{\Gamma_c^{(1)}(T_1,s)}\right] + I_{\infty,c}^{(2)}\left[1-\frac{\Gamma_c^{(2)}(T_2,s)}{\Gamma_c^{(1)}(T_1,s)}\right], \tag{3.13}$$

where $I_c^{(2)\mathrm{AP}}$ is the intensity at the synthesised aerial perspective that emulates the natural aerial perspective of “scene 2”.

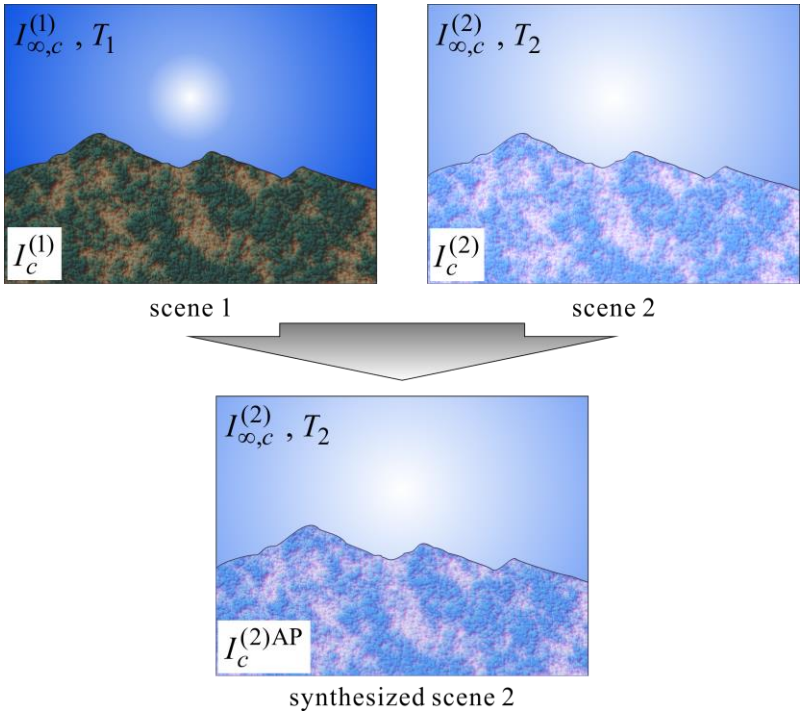

Figure 3.8. Scheme for rendering one synthesized scene based on two outdoor scenes.

We evaluated our aerial perspective rendering model formulated in Equation (3.13) using images of Tokyo city captured by Canon EOS 5D and applying our synthesized effect to the entire scene except the sky portion. We employed the real scene of T=1.9 of Figure 3.9 as "real scene 1". We used the depth map showed in Figure 3.9 and estimated from Google earth. Figure 3.10, Figure 3.11, and Figure 3.12 illustrate the results obtained by our method and by Zhao's method for different weather conditions of T=2.11, T=2.54, and T=4.36 respectivelly. As can be seen from the results, our method can generate more compelling appearances than Zhao's darker aerial perspective effect.

In order to numerically compare how similar two images are, general approaches make use of a histogram evaluation of the Hue Saturation Brightness (HSV) values of pixels. Therefore, we analyzed the similarity of "real scene 2" compared to the "synthesized scene 2" by calculating the following HSV histogram correlation:

$$Corr_{c}(H_1, H_2) = \frac{\sum_{c}(H_1(c) - \bar{H}_1)(H_2(c) - \bar{H}_2)}{\sqrt{\sum_{c}(H_1(c) - \bar{H}_1)^2 \sum_{c}(H_2(c) - \bar{H}_2)^2}}, \tag{3.14}$$

where H is histogram, $\bar{H}$ stands for the mean of the histrogram, c∈{H,S,V}, and lower indexes $_1$ and $_2$ correspond to the "real scene 2" and the "synthesized scene 2" respectivelly. *Corr*=1 means a perfect matching between "real scene 2" and the "synthesized scene 2". In fact, the higher the correlation between "real scene 2" and the "synthesized scene 2" is, the more similar they are.

Figure 3.9. Left: Real scene of Tokyo city (Atmospheric turbidity was estimated as T=1.9) captured by Canon EOS5D. Right: The corresponfing depth map.

"Real scene 2" (T=2.11)

"Synthesized scene 2" (T=2.11) with our rendering model

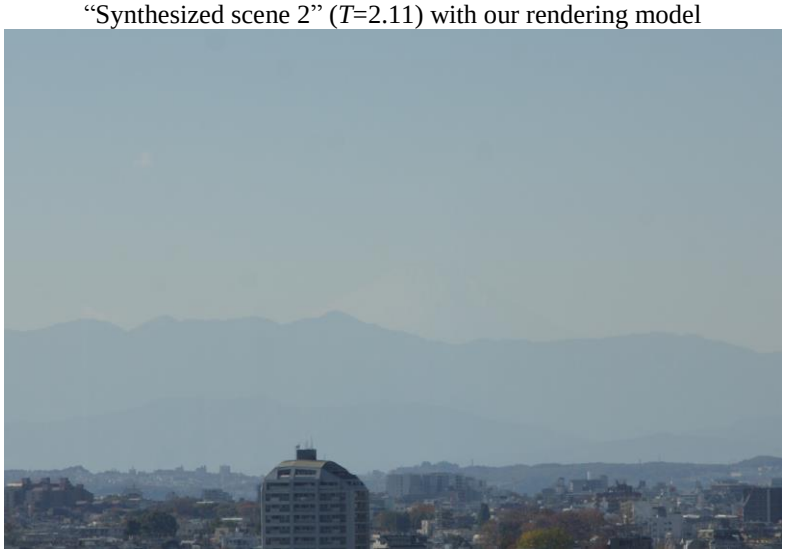

"Synthesized scene 2" (T=2.11) with Zhao's rendering model

Figure 3.10. Comparison among natural atmospheric effect, our aerial perspective effect, and Zhao's aerial perspective for scenes of T=2.11.

"Real scene 2" (T=2.54)

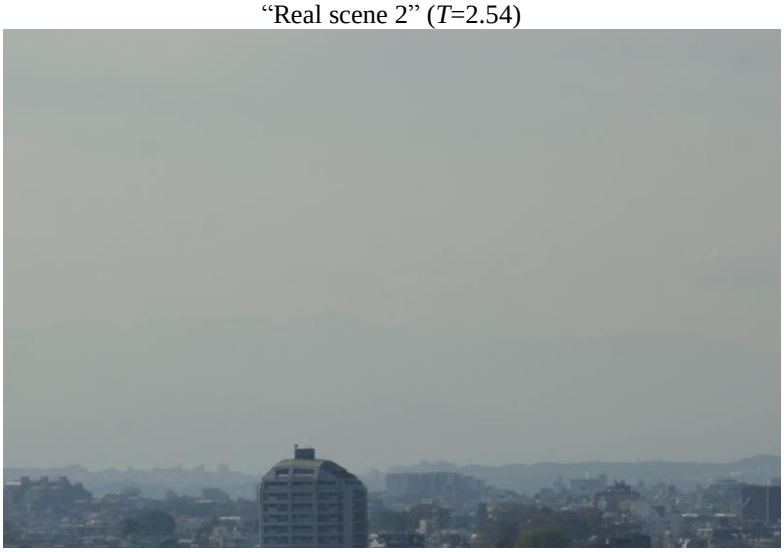

"Synthesized scene 2" (T=2.54) with our rendering model

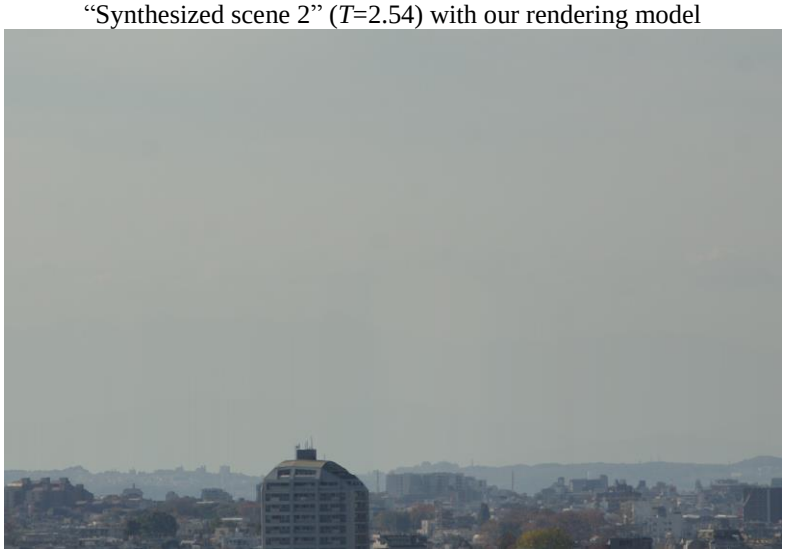

"Synthesized scene 2" (T=2.54) with Zhao's rendering model

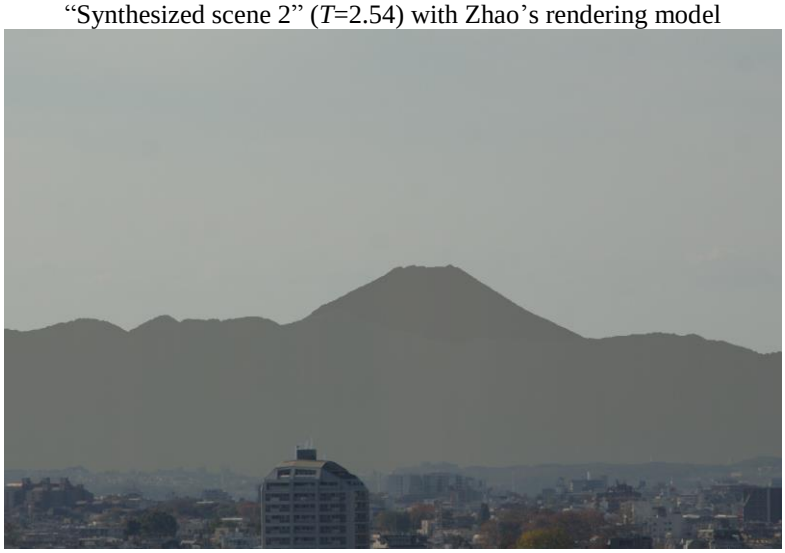

Figure 3.11. Comparison among natural atmospheric effect, our aerial perspective effect, and Zhao's aerial perspective for scenes of T=2.54.

“Real scene 2” (*T*=4.36)

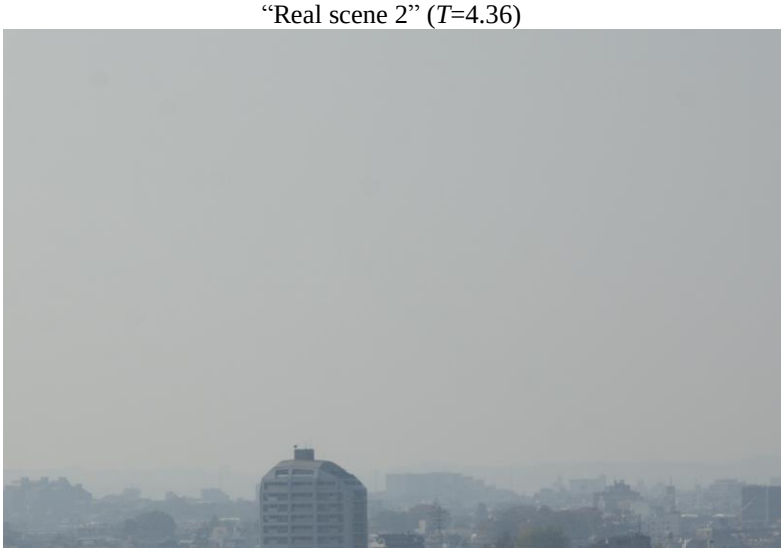

“Synthesized scene 2” (*T*=4.36) with our rendering model

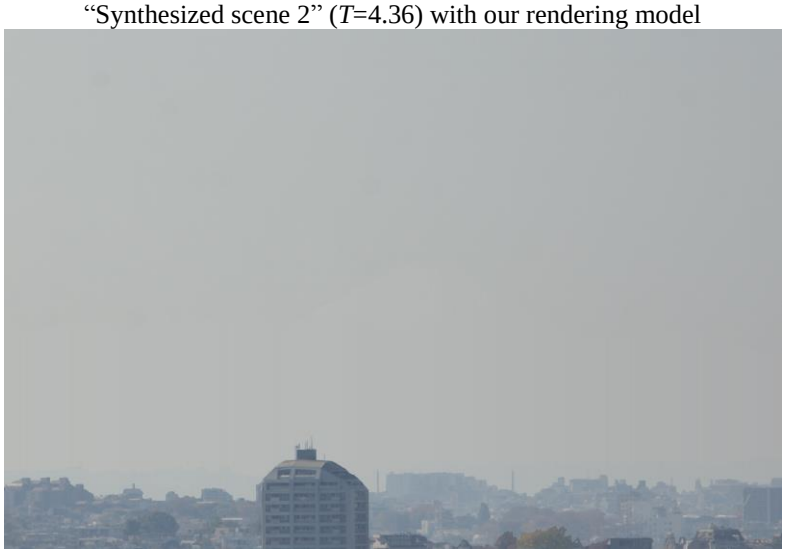

“Synthesized scene 2” (*T*=4.36) with Zhao’s rendering model

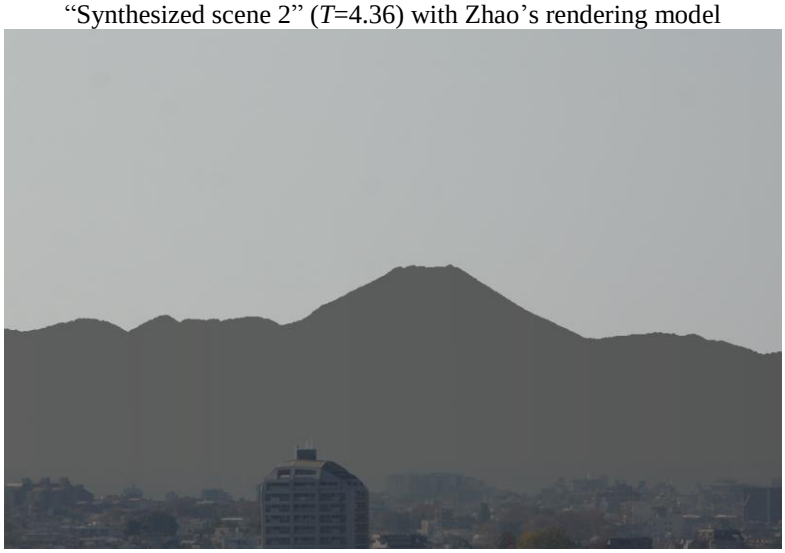

Figure 3.12. Comparison among natural atmospheric effect, our aerial perspective effect, and Zhao’s aerial perspective for scenes of *T*=4.36.

Figure 3.13 and Figure 3.14 illustrate the results obtained by applying Equation (3.14) to the "real scene 2" and the "synthesized scene 2" of Figure 3.10, Figure 3.11, and Figure 3.12 respectivelly. The results corroborate that our turbidity-based aerial perspective redering method has higher correlations with natural atmospheric effects than Zhao's method, thus proving to generate more compelling effects than Zhao's rendering model.

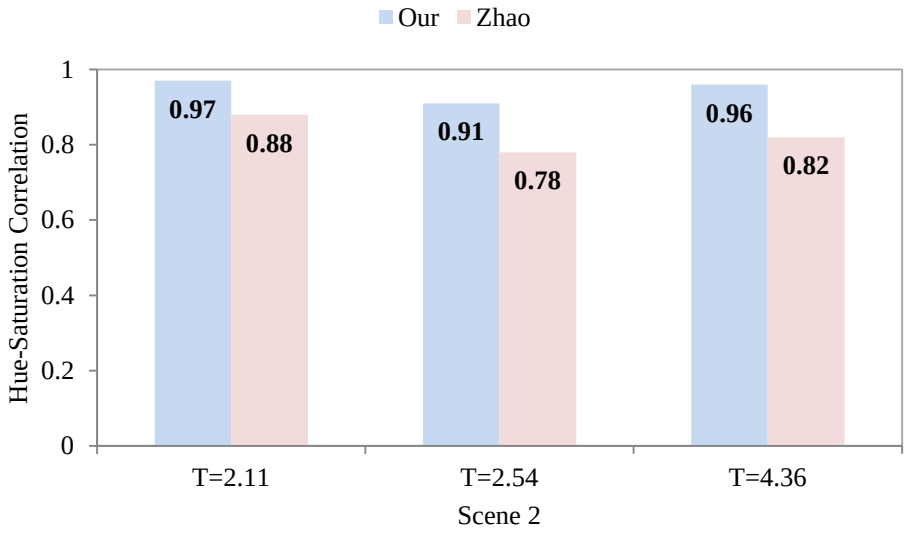

Figure 3.13. Hue-Saturation histogram correlation between "real scene 2" and the "synthesized scene 2" generated by our method and Zhao's method for various *T*.

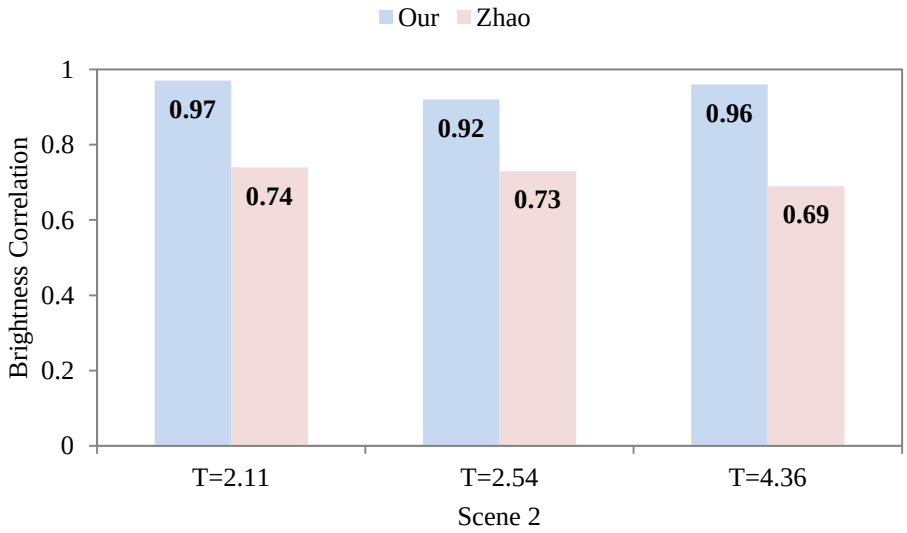

Figure 3.14. Brightness histogram correlation between "real scene 2" and the "synthesized scene 2" generated by our method and Zhao's method for various *T*.

3.5 Summary

We have proposed an improved scattering model directed to MR applications. Our corrections to previous scattering models are based on the widely-used experimental data provided by McCartney (1975). We have also analyzed the scattering model proposed by Zhao (2012) as he did some modifications on Preetham *et al*. (1999)'s scattering model in order to make it applicable to MR. We have compared our corrected scattering model with the one obtained by Zhao and proved that his approximate attenuation factor is bigger than ours. Our main contribution is that we formulated an improved scattering model based on experimental data instead of simply guessing a correction factor based on weather it works or not for only one specific case (Zhao, 2012). Another contribution is that we have formulated a scattering coefficient categotization via turbidity under various weather conditions. Finally, we have presented a turbidity-based aerial perspective rendering model for MR. We evaluated our rendering method with real scenes under different weather conditions and proved to obtain more realistic results than Zhao (2012).

Chapter 4

Virtual Object Rendering with Aerial Perspective Effect in MR

In this chapter, we apply the formulated turbidity-based aerial perspective model of Chapter 3 for rendering a virtual object with aerial perspective effect. As the virtual object w employed the Virtual Asukakyo (Ikeuchi, Virtual Asukakyo Project), which virtually restores the ancient capital of Japan, Asukakyo, to its original status by using MR technology. In order to evaluate the contribution of the present chapter in terms of realism of the generated appearance and the computational time, we also implement Zhao's aerial perspective model and compare the results achieved using our rendering method and the results obtained through his approach.

Figure 4.1. Virtual Asukakyo project (Ikeuchi Lab, Virtual Asukakyo Project).

4.1 Virtual Object Rendering with Aerial Perspective Effect for MR

We applied our rendering method to the Virtual Asukakyo project (Ikeuchi, Virtual Asukakyo Project). In order to evaluate our aerial perspective rendering method, we have analized two cases: *Aerial perspective effect over Virtual Asukakyo* and *Aerial perspective effect over entire MR*. In the first case we applied our aerial perspective effect only to the Virtual Asukakyo making use of the estimated turbidity obtained from the real scene. In the second case we applied the aerial perspective effect to the entire MR scene for various simulated atmospheric conditions through turbidity-based sky models. In both cases, the experimental settings were the same and are described as follows.

The far view needed to perceive the aerial perspective was obtained placing the observer in a small hill named Amakashioka, around 900m from Asukakyo (see Figure 4.2). Figure 4.14 illustrates the setting of our experiment. The omnidirectional image captured at Amakashioka using a Ladybug2 camera is illustrated in Figure 4.14. There the red box shows where Asukakyo lies. All the evaluations where done using a personal computer (OS: Windows 7; CPU: Corei7 2.93GHz; RAM: 16GB). We implemented our aerial perspective rendering method in C++ with OpenCV. Height at the observer position was estimated from Google earth as h_0=134m (above sea level). We estimated the depth map from Google earth but it can also be obtained using Vinh *et al*.'s method.

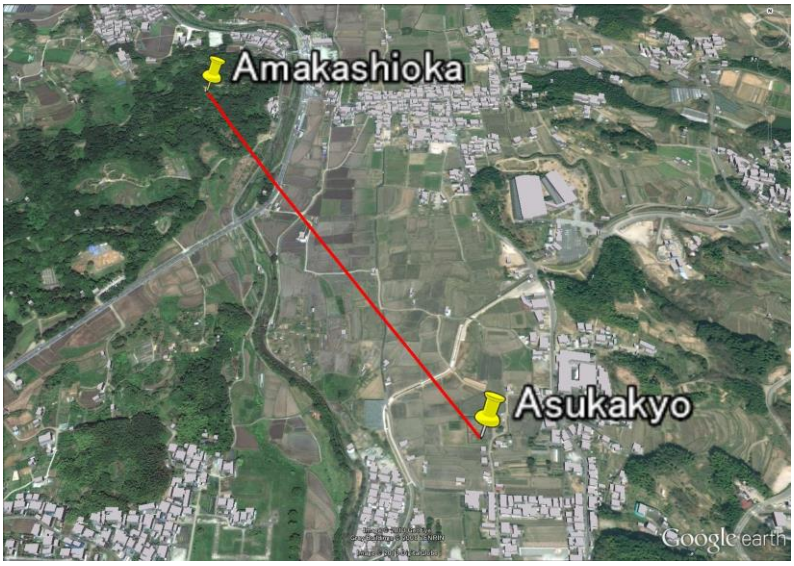

Figure 4.2. Asukakyo with respect of Amakashioka according to Google earth. Straight view Amakashioka-Asukakyo is about 900m.

Omnidirectional image from Amakashioka (*T*=1.87)

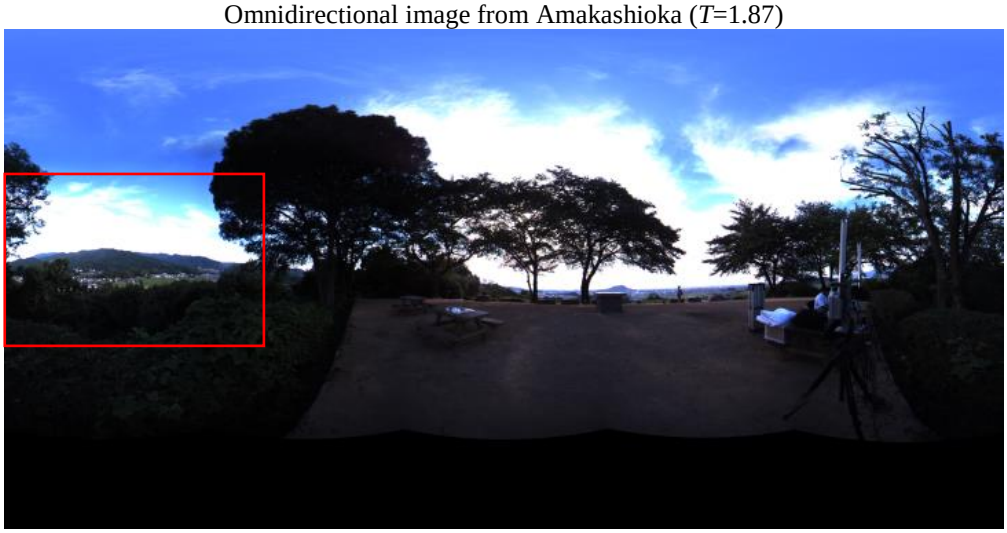

Real scene of Asukakyo (1400x1000 pixels)

Depth map of Asukakyo

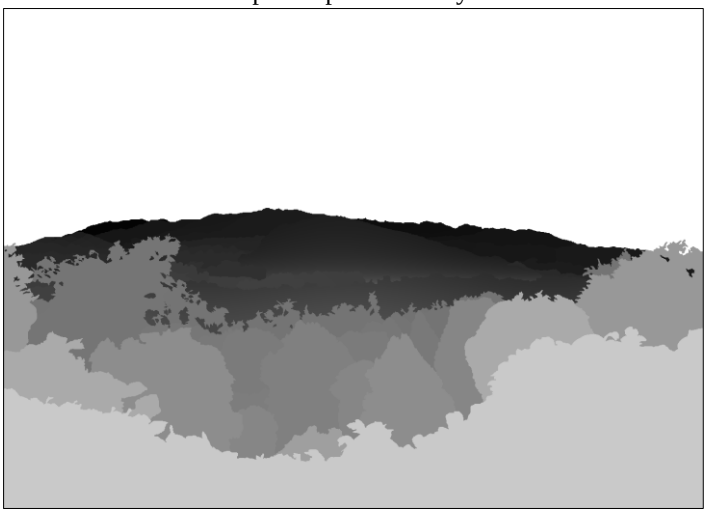

Figure 4.3. Experiment settings. Top: Image captured by Ladybug2 from Amakashioka (*T*=1.87). Middle: Real scene of Asukakyo city. Bottom: Depth map from Google earth.

Aerial perspective effect over Virtual Asukakyo: We first estimated the atmospheric turbidity T=1.87 of the real scene using our turbidity estimation method explained in Chapter 2. Then we rendered the Virtual Asukakyo with our aerial perspective effect and compared the result with Zhao's aerial perspective effect. Figure 4.4 shows the results of the evaluation. We observed that our rendering speed was 1800 pixels/sec (21 sec of total rendering time) and Zhao's rendering speed was 8pixels/sec (1h18min of total rendering time), thus proving that our rendering method is around 225 faster than Zhao's method.

From Figure 4.4 we can observe that the aerial perspective effect over the virtual object makes a whitening effect because of the white color of the environmental illumination. We also observe that there is not a so noticeable difference in the appearances generated by our method and Zhao's method; this is because the turbidity and the distance of the target do not generate a considerable RGB difference effect.

Aerial perspective effect over entire MR: We applied our aerial perspective effect to the entire MR scene for various simulated atmospheric conditions and compared our results implementing Zhao's aerial perspective effect for those atmospheric conditions. First, we obtained a scene without aerial perspective effect by applyring our rendering equation at the inverse. Then we simulated skies using Preetham sky models for different turbidities. Finally, we applied our aerial perspective effect and Zhao's atmospheric effect over the scene without aerial perspective effect. Figures 4.5-4.8 show the results of the evaluation.

From Figures 4.5-4.8 we can notice that our aerial perspective effect is more notorious and strong as the turbidity increases, while Zhao's aerial perspective effect does not change much even when going from low to high turbidities.

Without aerial perspective

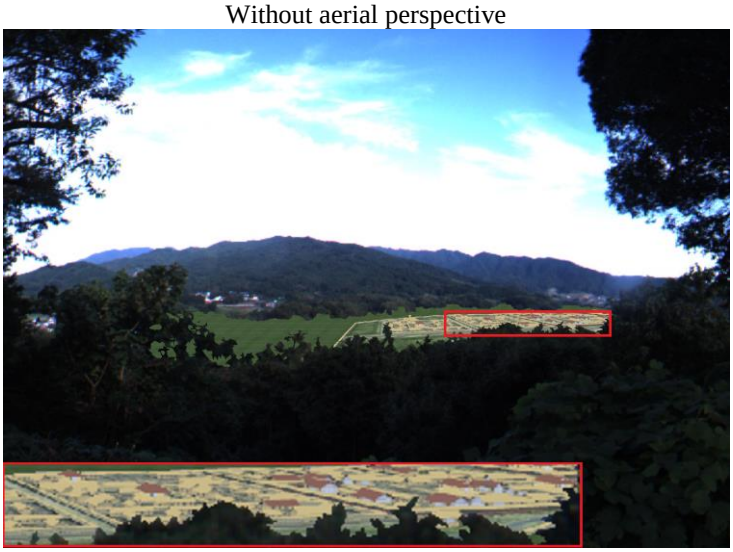

With our aerial perspective

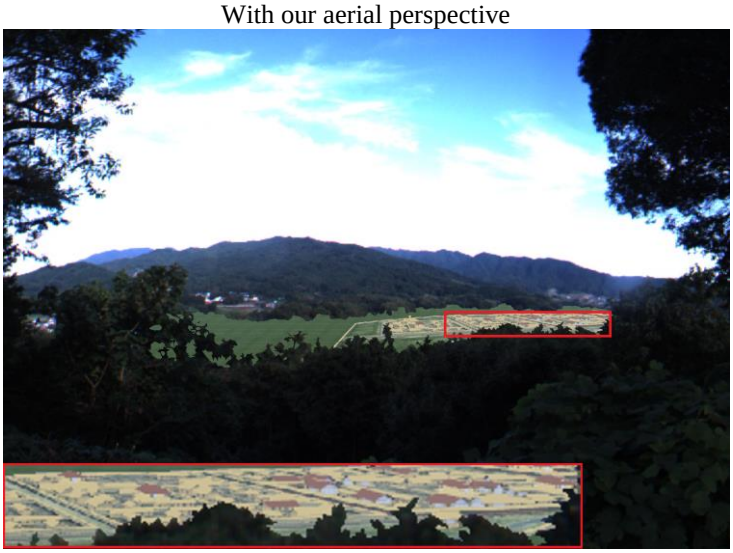

With Zhao’s aerial perspective

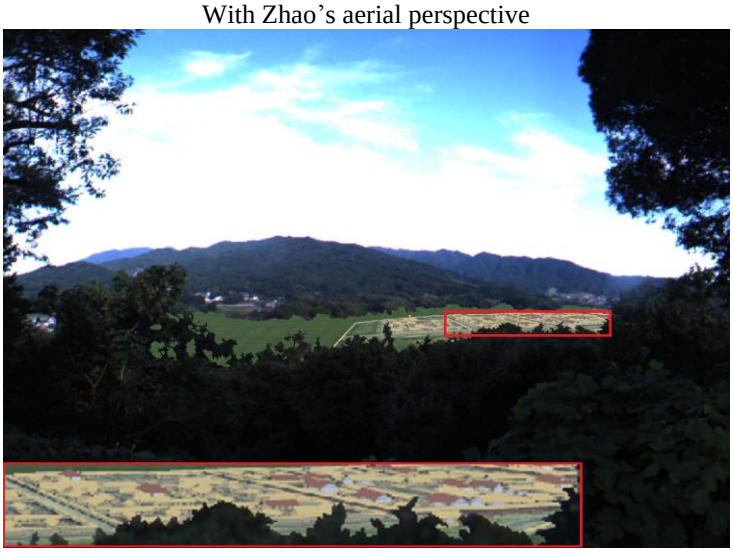

Figure 4.4. Virtual Asukakyo rendering. Top: without aerial perspective effect. Middle: our aerial perspective effect. Bottom: Zhao’s aerial perspective effect.

Our aerial perspective effect with simulated sky T=3

Zhao's aerial perspective effect with simulated sky T=3

Figure 4.5. Aerial perspective effect applied to the entire MR environment for simulated sky of T=3. Top: Rendering using our aerial perspective model. Bottom: rendering using Zhao's aerial perspective model.

Our aerial perspective effect with simulated sky T=5

Zhao's aerial perspective effect with simulated sky T=5

Figure 4.6. Aerial perspective effect applied to the entire MR environment for simulated sky of T=5. Top: Rendering using our aerial perspective model. Bottom: rendering using Zhao's aerial perspective model.

Our aerial perspective effect with simulated sky *T*=7

Zhao's aerial perspective effect with simulated sky *T*=7

Figure 4.7. Aerial perspective effect applied to the entire MR environment for simulated sky of *T*=7. Top: Rendering using our aerial perspective model. Bottom: rendering using Zhao's aerial perspective model.

Our aerial perspective effect with simulated sky *T*=9

Zhao's aerial perspective effect with simulated sky *T*=9

Figure 4.8. Aerial perspective effect applied to the entire MR environment for simulated sky of *T*=9. Top: Rendering using our aerial perspective model. Bottom: rendering using Zhao's aerial perspective model.

4.2 Summary

We have presented a fast turbidity-based aerial perspective rendering model for MR. We have rendered the Virtual Asukakyo with our aerial perspective effect and the results are more compelling that the results obtained using Zhao's aerial perspective effect. Another contribution lies in the computational cost of our rendering method, which is 225 times faster than Zhaos's method.

Chapter 5

Conclusions

5.1 Summary

In this thesis, we have proposed a fast and realistic turbidity-based method for rendering a virtual object with aerial perspective effect in MR.

In Chapter 2, we have proposed a fast turbidity estimation method that matches the luminance distribution of a sky model and the luminance distribution of an omnidirectional captured sky image. In comparison with Zhao (2012)'s RGB-based turbidity estimation approach, our luminance Y-based turbidity estimation method proved to be more robust to errors at sun position estimation.

In Chapter 3, we have proposed full-spectrum turbidity-based aerial perspective rendering model for MR applications. Our main contribution is that we have formulated an improved scattering coeffcients (for several atmospheric conditions) based on experimental data (McCartney, 1975), thus improving Zhao (2012)'s straightforward correction based on only one atmospheric condition with low turbidity. As a consequence of our corrected scattering model, we also provide a classification of scattering coefficients via turbidity. Besides, we have evaluated our aerial perspective rendering method with real scenes and our results proved to be more compelling in terms of appearance when compared with Zhao's darker aerial perspective effect.

In Chapter 4, we applied the proposed aerial perspective rendering model formulated in Chapter 3 to the Virtual Asukakyo project (Ikeuchi, Virtual Asukakyo Project). We rendered the Virtual Asukakyo with our aerial perspective effect and corroborated that Zhao's aerial perspective fails as it goes from low to high turbidity values. Another contribution is that our aerial perspective rendering speed is around 225 times faster than Zhao's model rendering speed.

5.2 Future Work

The proposed turbidity estimation method and aerial perspective rendering method for MR make a significant progress compared to previous works. Nonetheless, some issues still remain open.

Our turbidity estimation method cannot estimate turbidity in totally cloudy days where there are no visible clear-sky pixels. However, we could handle this issue by previously capturing one scene with known turbidity. We can use that scene to analyze the RGB values at some points different than the sky. Then we can compare those RGB values at those points with the values obtained at the same points but in the scene with cloudy sky. Assuming that the reflenctance properties of those points do not change through atmospheric conditions, the comparison can be carried out using our proposed aerial perspective model.

Besides, we can extend the flexibility of our turbidity estimation method by calculating the turbidity from an image taken by SmartPhone with the camera position and direction obtained by inertial sensors (GPS, electric compass, gravity sensor).

Our aerial perspective rendering speed proves to be faster than previous works (Preetham *et al.*, 1999; Zhao, 2012), however, did not reach real time under the personal computer's features used in the implementation. We plan to handle this issue by increasing that speed through the implementation of our method on GPU.

Human perception of realism in MR is always an important issue. For that purpose, we plan to conduct a user study experiment in order to verify people's perception of our aerial perspective effect over virtual objects.

Bibliography

A. Preetham, P. Shirley, and B. Smits. A practical analytic model for daylight. In *ACM Transactions on Graphics (SIGGRAPH)*, 1999.

B. Kristofor, T. Dung, and Q. Truong. An investigation of dehazing effects on image and video coding. IEEE TIP, 2012.

B. Vinh, T. Kakuta, R. Kawakami, T. Oishi, and K. Ikeuchi. Foreground and shadow occlusion handling for outdoor augmented reality. In *IEEE ISMAR*, pages. 109-118, 2010.

D. Lynch and W. Livingston. Color and light in nature. *Cambridge University Press*, 1995.

E. Goldstein. Sensation and perception. Wadsworth, 1980.

E. McCartney. Optics of the atmosphere: scattering by molecules and particles. *John Wiley and Sons*, 1975.

G. Meng, Y. Wang, J. Duan, S. Xiang, and C. Pan. Efficient image dehazing with boundary constraint and contextual regularization. In *ICCV'13*, pages 617-624, 2013

G. Mie. Beiträge zur Optik trüber Medien,speziell kolloidaler Metalllösungen. *Annalen der Physik 4*, 377–445, 1908.

G. Wyszecki and W. Stitles. Color science. Willey Interscience publication, 1982.

H. Zhao. Estimation of atmospheric turbidity from a sky image and its applications. *Ph.D dissertation*, The University of Tokyo, pages 13-30, 2012.

J. Haber, M. Magnor, and H. Seidel. Physically-based simulation of twilight phenomena. *ACM Transactions on Graphics 24*, 2005.

J. Kopf, B. Neubert, B. Chen, M. Cohen, D. Cohen-Or, O. Deussen, M. Uyttendaele, and D. Lischinski. Deep photo: model-based photograph enhancement and viewing. In *ACM SIGGRAPH Asia 2008*, 2008.

J. Tarel, N. Hautiere, A. Cord, D. Gruyer, and H. Halmaoui. Improved visibility of road scene images under heterogeneous fog. In *IV'10*, 2010.

K. He, J. Sun, and X. Tang. Single image haze removal using dark channel prior. In *CVPR'09*, pages 1956-1963, 2009

K. Ikeuchi. Virtual Asukakyo Project. http://www.cvl.iis.u-tokyo.ac.jp/research/virtual-asukakyo/

L. Hosek and A. Wilkie. An analytic model for full spectral sky-dome radiance. *ACM Transactions on Graphics*, vol. 31, No. 4, 2012

L. Kratz and K. Nishino. Factorizing scene albedo and depth from a single foggy image. In *ICCV'09*, pages 1701-1708, 2009.

L. Rayleigh. On the scattering of light by small particles. In *Philosophical Magazine 41*, pages 447-454, 1871.

M. Minnaert. Light and color in the open air. *Dover*, 1954.

OpenGL Documentation. OpenGL fog. http://www.opengl.org/documentation

R. Fattal. Single image dehazing. In *ACM SIGGRAPH 2008*, pages 72:1-72:9, 2008.

O. Elek and P. Kmoch. Real-time spectral scattering in large-scale natural participating media. In *Proceedings of Spring Conference on Computer Graphics*, 2010.

R. Habel, B. Mustata, and M. Wimmer. Efficient spherical harmonics lighting with the Preetham skylight model. In *Eurographics Association*, 2008.

R. Perez, R. Seals, and J. Michalsky. An all weather model for sky luminance distribution. *Solar Energy*, 1993.

R. Tan. Visibility in bad weather from a single image. In *CVPR'08*, pages 1-8, 2008.

S. Nayar and S. Narasimhan. Vision in bad weather. In *ICCV (2)*, pages 820-827, 1999.

S. Narasimhan and S. Nayar. Contrast restoration of weather degraded images. *IEEE TPAMI*, 25(6):713-724, 2003.

S. Narasimhan and S. Nayar. Vision and the atmosphere. In *IJCV*, pages 233-254, 2002.

S. Shwartz, E. Namer, and Y. Schechner. Blind haze separation. In *CVPR'06*, vol. 2, 2006.

T. Nishita, T. Sirai, K. Tadamura, and E. Nakamae. Dislpay of the earth taking into account atmospheric scattering. In *Proceedings of the 20th annual conference on Computer Graphics and Interactive Techniques, ACM, SIGGRAPH*, 1993.

T. Nishita, Y. Dobashi, and E. Nakamae. Dislpay of clouds taking multiple anisotropic scattering and sky light. In *Proceedings of the 23rd annual conference on Computer Graphics and Interactive Techniques, ACM, SIGGRAPH*, 1996.

Publication

C. Morales, H. Zhao, R. Kawakami, T. Oishi, and K. Ikeuchi. Turbidity-based aerial perspective rendering for mixed reality. In *Computer Vision and Image Media (CVIM 2014)*, Jan. 2014.